Spectroscopy of proton unbound states in ^{32}Cl

Mohamed Kamil

Faculty of Natural Sciences

Department of Physics & Astronomy

University of the Western Cape

A thesis submitted in partial fulfillment for the degree of

Master of Physical Sciences

2018

Declaration

I declare that "Spectroscopy of proton unbound states in ^{32}Cl",
is my own work, that it has not been submitted for any degree
or examination in any other university, and that all sources I
have used or quoted have been indicated and acknowledged by
complete references.

Mohamed Kamil   Month year

 Signature:

To my parents.

Acknowledgements

I would like to express my special thanks and gratitude to my supervisor Smarajit Triambak whose expertise, understanding, and patience added considerably to my graduate experience. I appreciate his vast knowledge and skill in many areas. I doubt that I will ever be able to convey my appreciation fully, but I owe him my eternal gratitude.

A very special thanks goes out to my co-supervisor Vicente Pesudo. He provided me with direction and technical support. He is a great teacher and friend.

I would also like to thank the K600 collaboration. Ricky Smit, Retief Neveling, Luna Pellegri, Paul Papka, Daniel Marin-Lambarri and Philip Adsley for their help and advice during the course of the experiment.

A very special thanks goes out to my colleagues at the University of the Western Cape nuclear physics group, Zandile Mabika, Lutendo Phuthu, Ndinannyi Mukwevho, Bhivek Singh and especially to Bernadette Rebeiro for her valuable suggestions and words of advice during my MSc.
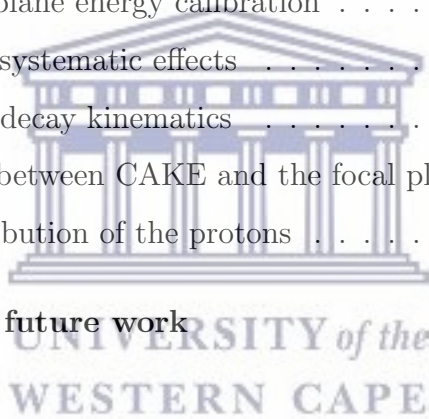
Abstract

This project aimed to investigate proton unbound states in ^{32}Cl using the ^{32}S(^{3}He, t) charge-exchange reaction. This research is relevant both in the context of nuclear structure and astrophysics. Excited states in ^{32}Cl up to $E_x \sim 6$ MeV were produced using a 50 MeV ^{3}He^{++} beam from the K200 separated sector cyclotron at iThemba LABS. The triton ejectiles were mass analysed and detected at the focal plane of the K600 magnetic spectrometer. An additional segmented silicon detector array called CAKE was used to detect the unbound protons from states in ^{32}Cl in conjunction with the tritons. In this work we looked for potential sources of isospin admixture that could explain the apparent violation of the Isobaric Multiplet Mass Equation (IMME) for the $A = 32, T = 2$ quintet. We also investigated the possibility of determining the ^{31}S(p, γ) reaction rate indirectly, via measurements of the partial proton widths of unbound states in ^{32}Cl.

Contents

i

ii

List of Figures

iv

UNIVERSITY *of the*
WESTERN CAPE

vii

Introduction

The main purpose of this project was to study proton unbound states in ^{32}Cl in order to better understand isospin symmetry violations in the $A = 32$, $T = 2$ isospin quintet. Furthermore, an attempt was made to indirectly determine the ^{31}S(p, γ) reaction rate, which is an important reaction for nuclear astrophysics. The summary of this thesis is below.

In the first chapter I describe the motivation for this work from a nuclear structure perspective. The theoretical background describing nuclear isospin and its violation in the form of the Isobaric Multiplet Mass Equation (IMME) is described in this chapter. I further motivate the reason to investigate the violation of the IMME for the $A = 32$, $T = 2$ quintet, which could be due to isospin mixing in ^{32}Cl. Thereafter, the aim was to experimentally probe for sources of admixtures in the ^{32}Cl nucleus.

In the second chapter I introduce the astrophysical relevance of ^{31}S(p, γ) resonances. Here I describe stellar nucleosynthysis, with particular focus on explosive phenomena such as novae and x-ray bursts. The ^{31}S(p, γ) reaction rate is important in this context as it influences the Si-P burning cycle. I then describe resonance reactions, and derive their cross section by means of scattering theory. Finally I also derive the mathematical expressions to calculate the stellar nuclear reaction rates using the cross section.

In the third chapter I explain the experimental techniques and apparatus

1

that were used to experimentally probe the ^{32}Cl states of interest.

In the fourth chapter I provide a detailed description of the data analysis procedure. Finally, I introduce a set of algebraic constraints that can be used to extract spins and parities of proton-unbound states from proton angular distribution measurements for other similar investigations. My conclusions are briefly described in the final chapter.

Chapter 1

Nuclear isospin and the IMME

1.1 Charge independence of nuclear forces

When the neutron was discovered in 1932, it was observed that it had the same spin quantum number and almost the same mass as the proton. In 1936, the analysis of pp and np scattering data revealed that if one takes into consideration the Coulomb force, the pp and the np nuclear force were almost equal in strength. Therefore, it was inferred that the nuclear force between any two nucleons is charge independent [1]. Later on, it was suggested by Heisenberg that protons and neutrons can be seen as different states of the same particle, the nucleon. Thus, a new quantum number was needed to label these two different representations of the nucleon. It was called isospin.

1.2 Isospin formalism

The introduction of isospin as a quantum number is a direct consequence of the charge independence of hadronic forces. From a mathematical point of view, the algebra of isospin and spin are identical [2]. Analogous to spin-$\frac{1}{2}$

particles, the isospin formalism treats the difference between a proton and a neutron similarly as the difference between spin-up and spin-down particles, with $S_z = \pm\frac{1}{2}$. As mentioned previously nucleons are labelled with the additional quantum number called isospin, denoted by $t = \frac{1}{2}$, with two possible projections along the third axis, $t_3 = \pm\frac{1}{2}$, representing neutrons and the protons respectively. This is shown in Figure 1.1. All the commutation
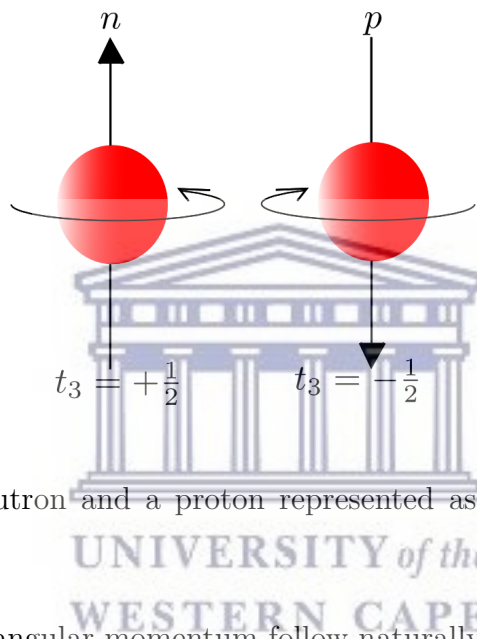
Figure 1.1: A neutron and a proton represented as projections in isospin space

relations for spin angular momentum follow naturally for isospin

$$[t_1, t_2] = it_3, \qquad [t_3, t_1] = it_2, \qquad [t_3, t_2] = it_1. \tag{1.1}$$

By the convention shown in Figure 1.1, the charge q of a nucleon is related to the third component isospin t_3, so that

$$q = e(\frac{1}{2} - t_3). \tag{1.2}$$

4

For atomic nuclei the total charge can be obtained by summing over all nucleons

$$Ze = \sum_{i=1}^{A} q_i = e(\frac{A}{2} - T_3), \qquad (1.3)$$

where,

$$T_3 = \sum_{i=1}^{A} t_{3,i}. \qquad (1.4)$$

From Eq. (1.3) it is obvious that

$$T_3 = \frac{A}{2} - Z = \frac{(N-Z)}{2}. \qquad (1.5)$$

It thereby follows that the isospin of nuclei are in the range

$$\frac{1}{2} \mid N - Z \mid \le T \le \frac{1}{2} A. \qquad (1.6)$$

If isospin were a good quantum number, the nucleon wave function would be invariant under rotations in isospin space. This symmetry leads to a conservation of the nucleon's mass, independent of its projection in isospin space.[1] This symmetry is obvious in pairs of mirror nuclei, which have the same mass number A, and different atomic number, with $Z_1 = \frac{1}{2}(A-x)$, and $Z_2 = \frac{1}{2}(A+x)$, where x is an integer. Observations have shown that mirror nuclei have similar binding energies and excitation energy spectra validating this symmetry (see Figure 1.2). If the symmetry was perfect in nature, these states should have identical masses, and they would be degenerate. Such states form part of an isospin multiplet.

---

[1]The mass difference between the u and the d quarks is neglected in this discussion and hereafter.

5
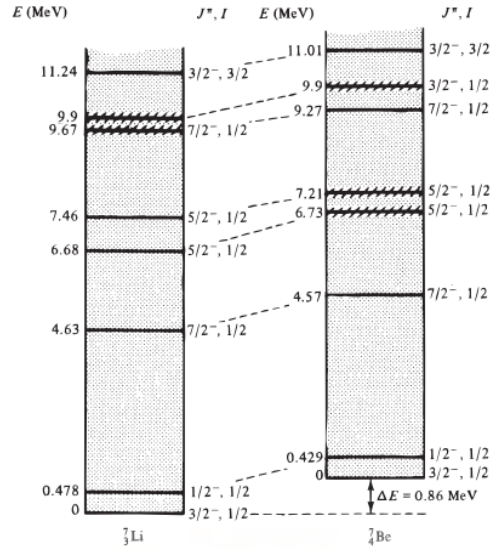
Figure 1.2: Level scheme for mirror nuclei, ^{7}Li and ^{7}Be. It should be noted that once electromagnetic corrections are taken into account, the energy levels in these nuclei are almost identical. Figure taken from Ref. [3]

.

1.2.1 Isospin symmetry breaking

It is well established that an external electromagnetic field breaks the degeneracy of energy levels in atomic nuclei (the Stark and Zeeman effects). Similarly, isospin symmetry is broken in nuclei by charge-dependent interactions. This results in the small difference between analogue levels in mirror nuclei, such as the ones shown in Figure 1.2. If one adds an electromagnetic Hamiltonian to the hadronic (charge independent) Hamiltonian so that

$$H = H_h + H_{em}, \tag{1.7}$$

then the breaking of isospin symmetry results in $[H, T] \neq 0$, i.e isospin not being a conserved quantity. It is apparent from Eq. (1.3) that the third component of isospin T_3 is directly related to the nuclear charge, which is a
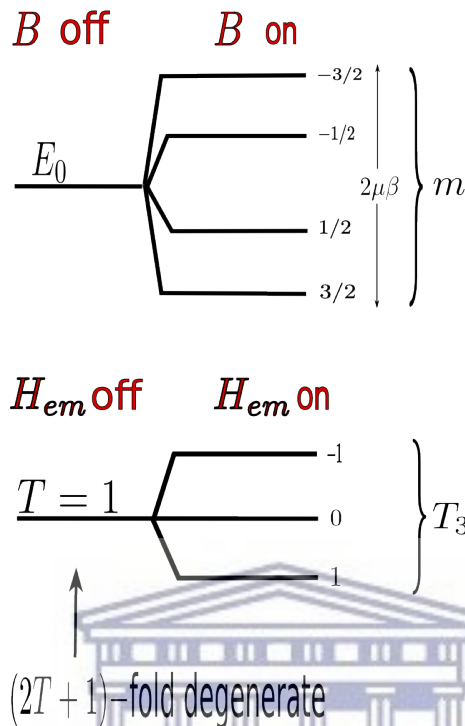
Figure 1.3: Breaking of a degeneracy by an external field.

conserved quantity. Therefore T_3 commutes with the Hamiltonian in Eq. (1.7) unlike T. States having the same quantum numbers (spin, parity, isospin, etc) that belong to neighbouring isobars are called isobaric analogue states (IAS). For a given isobaric multiplet with isospin T, there exist $(2T + 1)$ IAS which would be degenerate in the presence of purely charge independent hadronic forces. The $(2T + 1)-$fold degeneracy is lifted in the presence of charge-dependent interactions, so that the IAS are shifted relative to each other (see Figure 1.2 and Figure 1.3). These IAS belong to different nuclei (isobars) that are characterised by different projections T_3, for a given T. They have nearly identical masses and other similar nuclear properties based on the approximate symmetry of isospin. More specifically, isospin symmetry breaking in nuclei results from charge dependent perturbations which are re-

7

lated to T_3. In the most simple situation, the charge-dependent Hamiltonian in Eq. (1.7) can be expressed as a two-body Coulombic interaction, using Eq. (1.2)

$$H_{em} = e^2 \sum_{i<j} \left(\frac{1}{2} - t_3^i \right) \cdot \left(\frac{1}{2} - t_3^j \right) r_{ij}^{-1}. \tag{1.8}$$

This Hamiltonian can be expressed as a sum of isoscalar, isovector and an isotensor operator of rank 2 [4], so that

$$H_{em}^0 = \frac{1}{3} e^2 \sum_{i<j} \left(\frac{3}{4} + \vec{t^i} \cdot \vec{t^j} \right) r_{ij}^{-1}, \tag{1.9}$$

$$H_{em}^1 = \frac{1}{2} e^2 \sum_{i<j} \left(t_3^i + t_3^j \right) r_{ij}^{-1}, \tag{1.10}$$

$$H_{em}^2 = \frac{1}{3} e^2 \sum_{i<j} \left(3 t_3^i t_3^j + \vec{t^i} \cdot \vec{t^j} \right) r_{ij}^{-1}. \tag{1.11}$$

Now the T_3 dependencies can be factored out from the matrix element of H_{em} using the Wigner-Eckart theorem [4], so that the "reduced" expectation value of the electromagnetic Hamiltonian can be written as

$$E_{em}(A, T, T_3) = \sum_{k=0}^{2} (-1)^{T-T_3} \begin{pmatrix} T & k & T \\ T_3 & 0 & T_3 \end{pmatrix} \langle T || H_{em}^{(k)} || T \rangle. \tag{1.12}$$

Which results in a quadratic relation in T_3 for the Coulomb energies of the multiplet members

$$\begin{aligned} E_{em}(A, T, T_3) &= E_{em}^{(0)}(A, T) - T_3 E_{em}^{(1)}(A, T) \\ &\quad + (3T^2 - T(T+1) E_{em}^{(2)}(A, T), \end{aligned} \tag{1.13}$$

8

where, $E_{em}^{(0)}$, $E_{em}^{(1)}$ and $E_{em}^{(2)}$, are the scalar, vector and tensor Coulomb energies. The masses of the members of an isobaric multiplet are given by [4]:

$$M(A,T,T_3) = \frac{1}{2}(m_n + m_H)A + (m_n - m_H)T_3 + \langle TT_3|H_0|TT_3\rangle$$
$$+ \langle TT_3|H_1|TT_3\rangle + E_{em}(A,T,T_3)$$

(1.14)

Here:

- H_0 is the charge independent part of the Hamiltonian.

- The term linear in T_3, represents the difference between the electromagnetic self energies of the proton and neutron.

- All charge-dependent effects other than electrostatic interactions between protons and their-self energy are contained in $\langle TT_3|H_1|TT_3\rangle$.

- E_{em} is the Coulomb energy given in Eq. (1.13).

From Eq. (1.13) and Eq. (1.14) it can be easily seen that the masses of an isobaric multiplet satisfy the quadratic form

$$M(A,T,T_3) = a(A,T) + b(A,T)T_3 + c(A,T)T_3^2,$$

(1.15)

which is called the isobaric multiplet mass equation (IMME). The IMME has been a very successful tool in the past to predict masses and other observables where direct measurements were difficult. For example it has been used to map the proton drip line, determine the rp-processes path in stellar nucleosynthesis and to identify nuclei that decay with diproton emission [5]. Recently, together with shell model calculations, the IMME was used to deduce (p,γ) reaction rates relevant for stellar nucleosynthesis [6] and constrain

9

calculations of isospin mixing in $0^+ \to 0^+$ β-decays for fundamental tests of the electroweak interactions [7].

1.3   Isospin mixing in nuclei

Assume two states of the same spin and parity, but different isospin, represented by $|\phi_1\rangle$ and $|\phi_2\rangle$ (shown in Figure 1.4), that are separated by an energy difference ΔE_u. The energy eigenvalues of these nuclear states are represented by E_1 and E_2 respectively. In reality, these states are known to have admixtures of different configurations on account of the residual interaction, which can be treated as a perturbation. As a result of this perturbation,
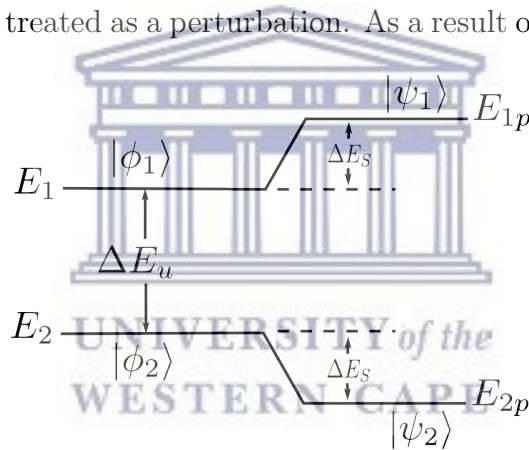
Figure 1.4: Two-state isospin mixing

.

the perturbed energy eigenvalues are obtained by diagonalising the matrix [8]

$$\begin{pmatrix} E_1 & V \\ V & E_2 \end{pmatrix},$$

(1.16)

where $\langle\phi_2|V|\phi_1\rangle$ is the isospin mixing matrix element. By defining a ratio

$$R = \frac{\Delta E_u}{\langle\phi_2|V|\phi_1\rangle},$$

(1.17)

10

one can obtain the perturbed energies in terms of the unperturbed levels E_1 and E_2,

$$E_{2p,1p} = \Big(\frac{E_1 + E_2}{2}\Big) \pm \frac{\Delta E_u}{2}\sqrt{1 + \frac{4}{R^2}}. \tag{1.18}$$

Its follows that, on account of the perturbations each energy eigenvalue is shifted by $|\Delta E_s| = |E_{1p} - E_1| = |E_{2p} - E_2|$, so that

$$|\Delta E_s| = \frac{\Delta E_u}{2}\Big[\sqrt{1 + \frac{4}{R^2}} - 1\Big]. \tag{1.19}$$

The isospin admixed states are given by

$$|\psi_1\rangle = \alpha|\phi_1\rangle + \beta|\phi_2\rangle, \tag{1.20}$$

$$|\psi_2\rangle = -\beta|\phi_1\rangle + \alpha|\phi_2\rangle, \tag{1.21}$$

where α and β are probability amplitudes, so that $\alpha^2 + \beta^2 = 1$ and $\beta = \frac{1}{\left(1 + \left[\frac{R}{2} + \sqrt{1 + \frac{R^2}{4}}\right]^2\right)^{\frac{1}{2}}}$. It is evident from Eq. (1.19) that the mixing between the states depends only on ΔE_u and the mixing matrix element $\langle\phi_2|V|\phi_1\rangle$. This describes briefly the algebra of isospin mixing in nuclei. The reason for this discussion will become evident in the section below.

1.3.1 The IMME for the $A = 32$ quintet

In general the quadratic form of IMME is expected to hold quite well for nuclei with $A < 40$. The IAS within these multiplets are unlikely to suffer from isospin mixing effects because of the relatively low level density in these nuclei. The $A = 32$, $T = 2$ quintet is one of the most precisely measured multiplets to date [9]. In this case a dramatic break-down of the IMME was reported, requiring an additional cubic term dT_3^3 with $d = 0.89 \pm 1.3$ keV to

11
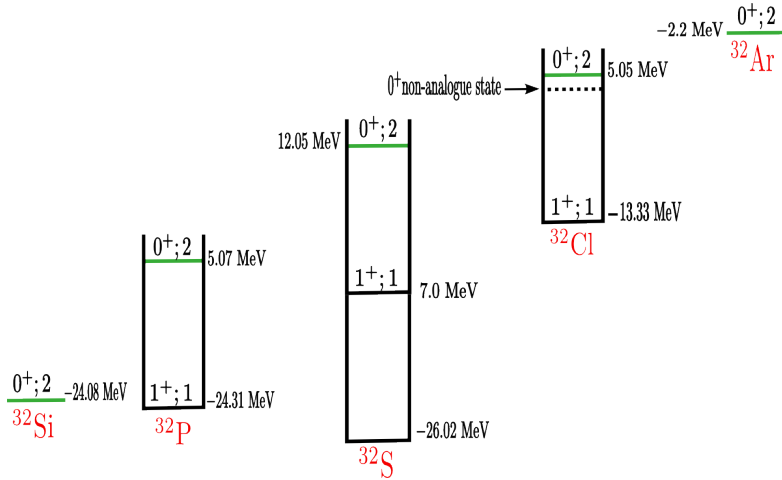
Figure 1.5: The $A = 32$, $T = 2$ quintet (green) and $T = 1$ triplet (black). The ground states are expressed in term of the mass excess.

obtain a reasonable fit to the data [10, 11]. The reason for this violation in the $A = 32$ quintet is still a mystery [12]. Potential reasons for this breakdown could be isospin mixing, the requirement for 3-body forces, or a higher-order perturbation theory etc. Recent shell model calculations have hinted at the possibility of a non-analogue 0^+ state in the vicinity of the $T = 2$, isobaric analogue state of ^{32}Cl that mixes with the IAS and leads to a breakdown of the IMME [13]. However this claim has not been experimentally verified yet. The calculations indicate the presence of a non-analogue 0^+ state ~ 73 keV around the IAS, with a mixing matrix element of $\langle \phi_2 | V | \phi_1 \rangle \sim 20$ keV [13]. This would lead to a shift in the energy of each state, $|\Delta E_s| \approx 6$ keV, resulting in a ratio of $R \approx 3$ from Eq. (1.17). This value quantifies the small shift in the energy of the 0^+ IAS due to isospin mixing with a non-analogue state that is separated from the IAS by ~ 73 keV. Such a shift can explain the requirement for a small cubic term with $d \sim 1$ keV for this particular multiplet. One of the main goals of this work is to look for this source of isospin admixture around the $T = 2$ state in ^{32}Cl (see Figure 1.5).

12

Chapter 2

Novae Nucleosynthesis and the $^{31}\mathrm{S}(p,\gamma)$ reaction

According to the standard Big Bang cosmology, the expansion and cooling of the early universe allowed for quarks to condense together to form nucleons. As the temperature further dropped to around 10^{11} K, the protons and neutrons remained in equilibrium interconverting through the weak interaction processes:

$$\overline{\nu}p \to e^+n, \qquad (2.1)$$

and

$$\nu n \to e^-p. \qquad (2.2)$$

As expansion of the universe continued, 1 s after the big bang the temperature dropped to $\sim 10^{10}$ K. The neutron to proton ratio froze out at this instant with the ratio 1 : 6 [14]. This is because the weak interaction rates shown above become slower than the expansion rate and the small neutron-proton mass difference favors proton production to neutrons. This ratio gradually gets worse for the neutrons as they further β decay to stable protons. Fur-

13

ther fusion of the excess protons (or hydrogen nuclei) leads to the formation of helium. Basically all the hydrogen and helium that exist in the universe originate from this Big Bang nucleosynthesis era [1].

So far the universe is made of hydrogen and helium gas scattered all over the space. In the regions of sufficiently dense clouds of matter, the gravitational force initiates collisions within the gas core, thus increasing its temperature [1]. This allows the hydrogen at the core to overcome the Coulomb barrier and fuse into helium, which eventually forms a main sequence star [15]. When the hydrogen in the star is completely exhausted, the star begin to contract due to the absence of an outward radiation pressure. The gravitational contraction of the star leads to a further increase in the temperature, making it possible to fuse helium into heavier elements [16]. This thermonuclear burning continues as long as sufficient fuel is available. A small fraction of the helium remains that undergoes a series of nuclear reactions producing carbon, oxygen, neon, etc [15, 16]. In this process, the star keeps piling up shells of elements in an onion-like structure with the higher mass elements closer to the core, as shown in Figure 2.1. The core of the most massive stars comprises of iron, which has the maximum binding energy per nucleon of all elements, as shown in Figure 2.2. Consequently, the unavailability of energy to fuse ^{56}Fe to make heavier elements stops this nucleosynthesis process at the iron group [1]. It is now understood that elements beyond ^{56}Fe are formed by slow and rapid neutron capture reactions (s- and r-processes), where the neutron abundances are produced in events such as short-lived violent supernovae [15] or neutron star mergers [18].

---

[1]The remaining heavier elements are formed much later, via stellar and supernovae nucleosynthesis.

14
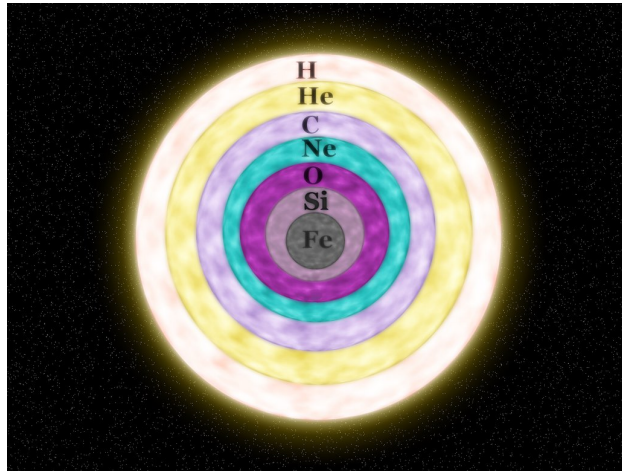
Figure 2.1: Elemental abundances in a stellar interior. Figure taken from [17].
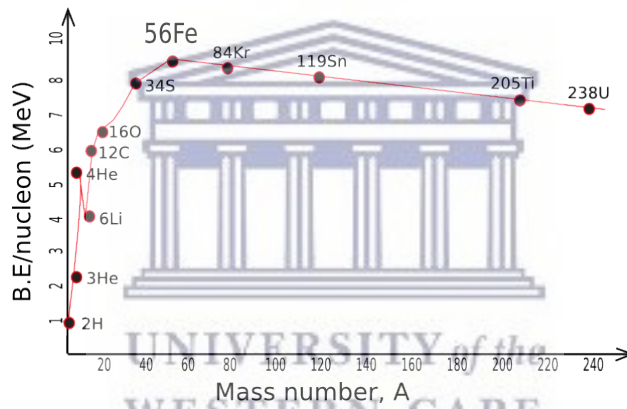
Figure 2.2: Binding energy per nucleon vs atomic mass. ^{56}Fe is the most stable element since it has the maximum binding energy per nucleon.

2.1 Novae and supernovae

The atoms in the stellar core are completely ionized and the free electrons form a highly degenerate gas. In some cases the degeneracy pressure balances the gravitational contraction even after the fuel in the inner shell is exhausted, thereby halting further stellar collapse. Such stars are called white dwarfs. At this stage if the mass of the star is greater than the Chandrasekhar limit $M > 1.44\ M_{\odot}$ ($M_{\odot}$ being the mass of the Sun), the electron degeneracy

15

pressure is not enough to prevent further gravitational collapse. The electrons fuse with protons forming neutrons, and these can not β-decay because the resulting electrons will have no states to populate, collapsing the core into nucleon gas, which leads to the formation of black holes or neutron stars [15]. For massive stars with $M \geq 8\ M_\odot$, gravitational contractions can lead to further burning of the remaining small amount of nuclear fuel and collapse of the stellar core. The photodisintegration of iron nuclei and further cooling by escaping neutrinos speed up the collapse, leading to a violent explosion that is called a Type II or core-collapse supernova [15].

2.1.1 Binary systems: Type I supernovae, novae and X-ray bursts

A binary star system usually consists of a hydrogen-rich young star and an older, highly dense star that is usually a white dwarf or a neutron star [15, 16]. The stars interact gravitationally, thus allowing for accretion of matter from the younger companion onto the surface of the older star which initiates thermonuclear reactions (Figure 2.3). These reactions occur because the ac-

Figure 2.3: A binary star system. Figure is taken from [19]

16

creting hydrogen-rich material accumulates on the surface of the older (dense) star and eventually becomes degenerate matter, which resists further compression. This degeneracy pressure prevents cooling as transitions to lower energy quantum states are not possible. As a result, the temperature on the surface of the dense star increases rapidly, leading to uncontrolled reactions called a thermonuclear runway [15, 20]. This results in a rapid increase in the luminosity of the star up to about $\sim 10^5$ solar luminosities. These phenomena are called classical novae, which can last for months or years before they fade. If the white dwarf gains mass that exceeds the Chandrasekhar limit due to the accretion process, the white dwarf collapses in a violent explosion, called a type I supernova [15]. Similar to classical novae, X-ray bursts originate from binary systems that include a neutron star (or a black hole) instead of the white dwarf. As material accretes on to the much denser neutron star, this results in periodic bursts of X-rays from the impact of the accreted material at very high velocities [16, 20].

2.2   Resonances and nuclear reaction rates

The burning process of the fuel in stars follow sequences of specific nuclear reaction cycles such as the C-N-O, Ne-Na, Mg-Al and Si-P, cycles [21, 22], shown in Figure 2.4. These cycles consist of proton capture reactions that compete with β decays and are enclosed by (p, α) reactions. Breakout reactions that link any two cycles are feasible due to (p, γ) resonant and direct capture reactions. The time scale of novae depends on such (p, γ) reaction rates. As mentioned above, these reactions can proceed via both non-resonant and resonant capture reactions. For non-resonant reactions, the incident proton can be represented by a plane wave, that interacts with a

17
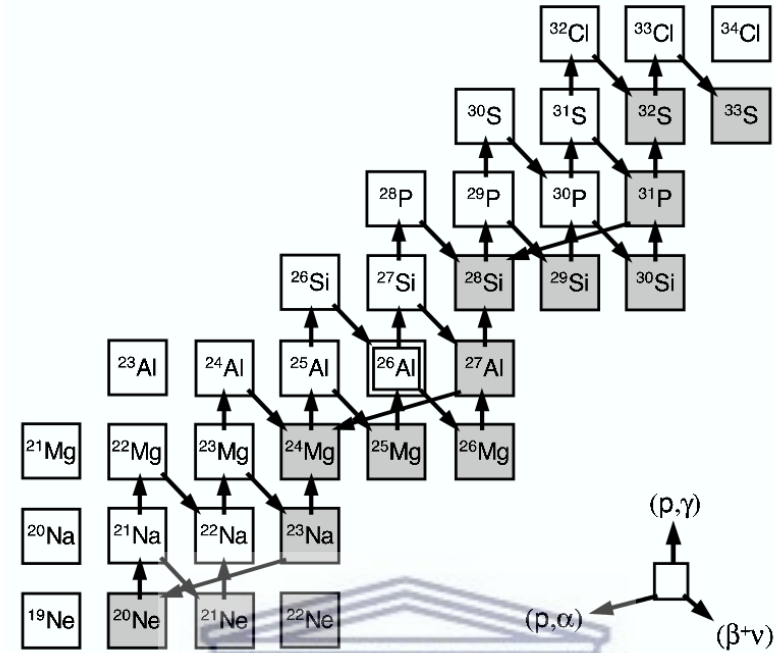
Figure 2.4: The Ne-Na, Mg-Al, and Si-P cycles. Figure is taken from [16].

target A, and directly populates a standing wave in a final compound nuclear state B [23]. Similar to bremsstrahlung, in this process a photon is emitted with energy $E_\gamma = E_p + Q - E_i$. Here E_p is the proton energy in the center of mass frame, Q denotes the reaction Q-value, and E_i is any excitation energy in the compound nucleus. The cross section for γ-ray production in such a reaction is characterised by the matrix element [15]

$$\sigma_\gamma \propto |\langle B|H_\gamma|A + p\rangle|^2. \tag{2.3}$$

In the above H_γ is an electromagnetic operator, which mediates the transition from the initial $|A + p\rangle$ state to the final state B. Such capture processes are governed by one matrix element, and hence called one-step or direct reactions [15], as shown in Figure 2.5. This sort of (p, γ) reactions are non-resonant reactions as they take place for all projectile energies. On the other

18
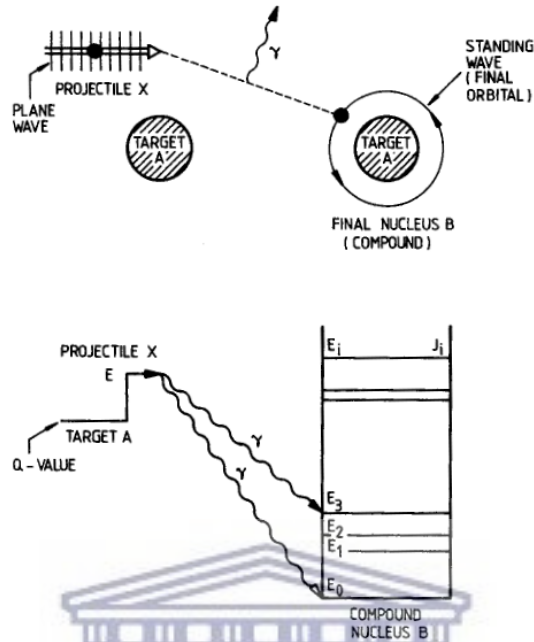
Figure 2.5: $A(X, \gamma)B$ direct capture reaction. Figure is taken from [15].

hand, a resonant (p, γ) reaction is a two-step process and is highly sensitive to the incident proton energy. In these reactions the incident proton first populates an excited state E_0 in the compound nucleus. Later, the state decays to a final excitation energy E_f, emitting a γ-ray. The probability for such a reaction is the product of the matrix elements for these two steps [15]

$$\sigma_\gamma \propto |\langle E_f | H_\gamma | E_0 \rangle|^2 |\langle E_0 | H_f | A + p \rangle|^2. \tag{2.4}$$

In the above, H_f is an operator that acts on the initial state $|A + p\rangle$ and creates an excited state E_0 in the compound nucleus, while H_γ is an operator that leads to the later γ decay. Because the reaction is governed by two matrix elements, it is considered to be a two-step reaction (Figure 2.6). The resonant reaction is sensitive to the projectile energy at the entrance channel.

19

The total energy at the entrance channel $Q + E_p$ must match the excitation energy E_0 in the compound nucleus for the reaction to occur [15]. The cross section for such reactions maximizes near well defined resonances. The cross section varies smoothly as a function of energy with intercepting resonances, depending on the width of the states involved, as illustrated below.

Lets consider a deexcitation from an excited state with decay constant λ.
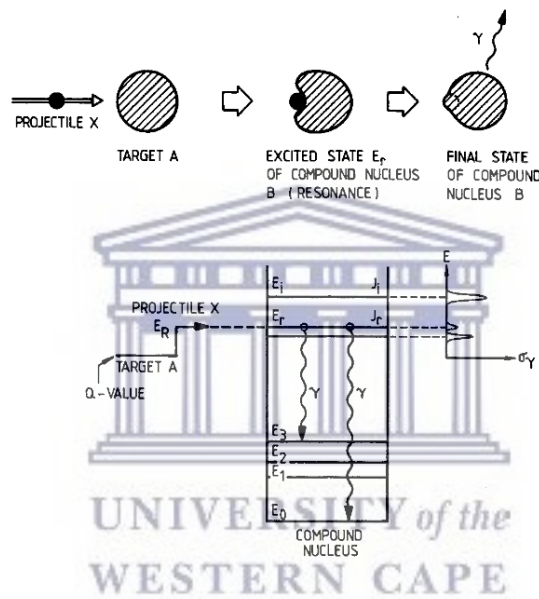
Figure 2.6: $A(X, \gamma)B$ resonant capture reaction. Figure is taken from [15].

The decay process is described by the well known exponential decay law

$$N(t) = N(0) \exp\big(-\lambda t\big), \tag{2.5}$$

where, $N(t)$ is the number of nuclei remaining in the excited state after a time t and $N(0)$ is the initial number of states at $t = 0$. The average time τ to exist in the excited compound nuclear state before it decays is related to the probability λ so that

$$\tau = \frac{1}{\lambda} = \frac{t_{1/2}}{\ln 2}, \tag{2.6}$$

20

where $t_{1/2}$ is the half-life of the state. We now focus on how to describe the time evolution of this decaying state. In general, it can be described as the stationary state solution

$$\Psi(t) = \Psi(0) \exp\left(-\frac{iEt}{\hbar}\right), \qquad (2.7)$$

so that the probability of finding the particle is conserved

$$|\Psi(t)|^2 = |\Psi(0)|^2, \qquad (2.8)$$

However, to allow the state to decay, one requires the addition of a small imaginary part to the energy, so that [1]

$$E = E_0 - \frac{1}{2}i\Gamma, \qquad (2.9)$$

where the $\frac{1}{2}$ factor is introduced for convenience. The above yields the probability

$$|\Psi(t)|^2 = |\Psi(0)|^2 \exp\left(-\frac{\Gamma t}{\hbar}\right), \qquad (2.10)$$

which agrees with the exponential decay law only if

$$\Gamma = \lambda\hbar. \qquad (2.11)$$

Therfore, the wave function of a decaying state can be correctly expressed as

$$\Psi(t) = \Psi(0) \exp\left(-\frac{iE_0 t}{\hbar}\right) \exp\left(-\frac{\Gamma t}{2\hbar}\right). \qquad (2.12)$$

Note, the wave function in the above equation is a function of time. Since we aim to get the probability of finding an emitted particle (photon) with en-

21

ergy E. This requires a Fourier transform from the 'time' domain to the 'frequency' domain, so that

$$g(\omega) \propto \Psi(E) = \frac{\Psi(0)}{\sqrt{2\pi}} \int_0^\infty dt \ \exp\left(i(\omega - \frac{E_0}{\hbar})t\right) \exp\left(\frac{\Gamma t}{2\hbar}\right), \qquad (2.13)$$

where the lower limit of the integration is set to zero assuming that the decay started at $t = 0$. Since $E_0 = \hbar\omega_0$, this yields

$$g(\omega) = \frac{\Psi(0)}{\sqrt{2\pi}} \int_0^\infty dt \ \exp\left(i(\omega - \omega_0 + i\frac{\Gamma}{2\hbar})t\right), \qquad (2.14)$$

whose solution gives us the amplitude

$$g(\omega) = \frac{\Psi(0)}{\sqrt{2\pi}} \left[\frac{i}{\omega - \omega_0 + \frac{i\Gamma}{2\hbar}}\right]. \qquad (2.15)$$

Therefore, the probability of emitting a particle with energy E should be $|g(\omega)|^2$, so that

$$P(E) = \frac{N}{2\pi} \frac{\hbar^2|\Psi(0)|^2}{(E - E_0)^2 + \Gamma^2/4}, \qquad (2.16)$$

where N is a normalization factor $= \frac{\Gamma}{\hbar^2|\Psi(0)|^2}$. This results in

$$P(E) = \frac{\Gamma}{2\pi} \frac{1}{(E - E_0)^2 + (\Gamma/2)^2}, \qquad (2.17)$$

which is called a Cauchy or Breit-Wigner distribution to describe the state, shown in Figure 2.7. The width of this distribution Γ, is related to the mean lifetime τ from Eq. (2.11) such that

$$\Gamma\tau = \hbar. \qquad (2.18)$$

This relation shows that decaying states have widths and that broad states have short lifetimes and vice-versa. Thus, the small complex energy term that we added in Eq. (2.9) had two effects

- It allowed for transitions to other eigenstates.

- It led to a broadening of the state.
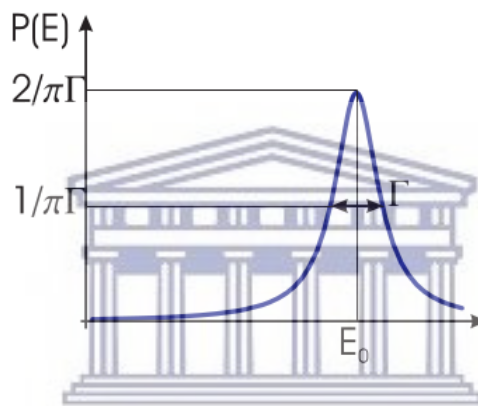
Figure 2.7: A Breit-Wigner distribution of width Γ. Figure is taken from [1].

Since the matrix elements in Eq. (2.4) are proportional to the probability of creating a new state E_0, and the probability for this state to decay to a final state E_f respectively, the two process can be represented by partial widths Γ_i for each process. Thus Eq. (2.4) can be rewritten as [15]

$$\sigma_\gamma \propto \Gamma_p \Gamma_\gamma. \tag{2.19}$$

2.2.1 Relation to nuclear reaction rates

In general, the measurement of a nuclear reaction rate requires a knowledge of the number of interactions between incident and target particles per unit

23

volume per unit time. This is governed by the cross section σ of the reaction. We now investigate the meaning of this cross section in more detail using scattering theory, within a non-relativistic context. For simplicity we assume a scattering process between spinless incoming particles and the target particles, with a central potential. The stationary state solutions to such a problem can be described as

$$\Psi(\vec{r}) = \Psi_{inc}(\vec{r}) + \Psi_{scat}(\vec{r}), \tag{2.20}$$

where $\Psi_{inc}(\vec{r})$ and $\Psi_{scat}(\vec{r})$ are the wave functions describing the incident and the scattered particles respectively. It is well established that in the limit $r \to \infty$, the solutions take the form

$$\Psi_{inc}(\vec{r}) + \Psi_{scat}(\vec{r}) \stackrel{r \to \infty}{=} e^{i\vec{k}.\vec{r}} + \frac{e^{ikr}}{r} f(k, \theta), \tag{2.21}$$

where $f(k, \theta)$ is a modulating factor called the scattering amplitude. One can then separate the incoming plane wave into a radial part and an angular part (taking into consideration the azimuthal symmetry) so that $e^{i\vec{k}.\vec{r}} = e^{ikz}$, and

$$e^{ikz} = \sum_{l=0}^{\infty} (2l + 1) i^l j_l(kr) P_l(\cos \theta) \tag{2.22}$$

for all partial waves of orbital angular momentum l. The total wave function can now be written as

$$\Psi(r, \theta) = \sum_{l=0}^{\infty} (2l + 1) i^l j_l(kr) P_l(\cos \theta) + f(\theta) \frac{e^{ikr}}{r}$$
$$= \sum_{l=0}^{\infty} b_l R_l(kr) P_l(\cos \theta), \tag{2.23}$$

24

which is further separated into radial and angular parts. Given the boundary conditions $(r \to \infty)$, the solution to the radial part is simply the Bessel function $j_l(kr) = \frac{\sin(kr-\frac{l\pi}{2})}{kr}$ [2]. $R_l(kr)$ will have a similar form except with a phase shift δ_l, so that $R_l(kr) = \frac{\sin(kr-\frac{l\pi}{2}+\delta_l)}{kr}$. Putting in the above explicitly, and rearranging coefficients, we get

$$
\Psi(r,\theta) = e^{ikr}\left[\sum_{l=0}^{\infty}\left\{\frac{(2l+1)}{2i}i^l\ e^{-i\frac{l\pi}{2}} - \frac{b_l}{2i}e^{-i\frac{l\pi}{2}}e^{i\delta_l}\right\}P_l(\cos\theta) + f(\theta)k\right]
$$
$$
+ e^{-ikr}\left[\sum_{l=0}^{\infty}\left\{-\frac{(2l+1)}{2i}i^l\ e^{i\frac{l\pi}{2}} + \frac{b_l}{2i}e^{i\frac{l\pi}{2}}e^{-i\delta_l}\right\}P_l(\cos\theta)\right] = 0.
$$

$$(2.24)$$

Equating coefficients on the LHS and RHS, one can obtain after some algebra

$$
b_l = (2l+1)i^l\ e^{i\delta_l}.
$$

$$(2.25)$$

On back substituting this value, the scattering amplitude can be evaluated as

$$
f(\theta) = \frac{1}{k}\sum_{l=0}^{\infty}(2l+1)e^{i\delta_l}\sin\delta_l P_l(\cos\theta).
$$

$$(2.26)$$

This scattering amplitude is an experimentally measurable quantity and relates directly to the differential scattering cross section

$$
\frac{d\sigma}{d\Omega} = |f(\theta)|^2,
$$

$$(2.27)$$

so that total cross section σ is

$$
\sigma = 2\pi\int_{-1}^{1}|f(\theta)|^2\ .\ d(\cos\theta).
$$

$$(2.28)$$

25

Using the orthonormality of the $P_l(\cos\theta)$ we get this cross section to be simply

$$\sigma = \frac{4\pi}{k^2} \sum_{l=0}^{\infty} (2l+1)\sin^2\delta_l. \qquad (2.29)$$

Clearly the scattering cross section is maximum when the lth partial wave undergoes a phase shift of $\frac{\pi}{2}$, from Eq. (2.29).

At this stage the cross section $\sigma \propto \sin^2\delta_l$ can also be expanded as

$$\sigma \propto \frac{1}{1 + \cot^2\delta_l}. \qquad (2.30)$$

On Taylor expanding $\cot\delta_l(E)$ about $E_p = E_0$, we get

$$\begin{aligned}\cot\delta_l(E) &= \cot\delta_l(E_0) + (E - E_0)\left(\partial_E\cot\delta_l\right)\bigg|_{E=E_0} + \dots \ , \\ &= \left(\frac{-1}{\sin^2\delta_l}\frac{d\delta_l}{dE}\right)_{E=E_0}(E - E_0) + \dots \ . \end{aligned} \qquad (2.31)$$

Since we assume at the resonance $\delta_l(E_0) = \frac{\pi}{2}$, the $\cot\delta_l(E_0)$ term in the first line vanishes and $\frac{-1}{\sin^2\delta_l} = -1$. Furthermore we can arbitrary define $(\frac{d\delta_l}{dE})_{E=E_0} = \frac{2}{\Gamma}$ so that the above equation can be rewritten as

$$\cot\delta_l(E) = -\frac{2}{\Gamma}(E - E_0) = -\frac{(E - E_0)}{\frac{\Gamma}{2}}. \qquad (2.32)$$

Substituting the phase shift value into Eq. (2.29), we get

$$\sigma = \frac{\pi}{k^2}(2l+1)\frac{\Gamma^2}{(\Gamma/2)^2 + (E - E_0)^2}. \qquad (2.33)$$

Since the (p, γ) reaction is a two-step process (the creation of the state and the later decay), the Γ^2 in the numerator can be replaced by the product of the two probabilities Γ_p and Γ_γ. Finally on incorporating spin and orbital

26

angular momentum, the cross section is weighted with a statistical factor [16]

$$g = \frac{(2J+1)}{(2l+1)(2S_a+1)(2S_b+1)}, \qquad (2.34)$$

where J is angular momentum of the final state. S_a and S_b are the spins of the incident and the target particles, and l is the transferred orbital angular momentum. Finally we can get the value of the cross section for $l = 0$ (s-wave scattering) to be

$$\sigma(E) = \pi\lambda^2\omega\frac{\Gamma_p\Gamma_\gamma}{(\Gamma/2)^2 + (E - E_0)^2}, \qquad (2.35)$$

with $\omega = \left(\frac{(2J+1)}{(2S_a+1)(2S_b+1)}\right)$ and $\lambda = \frac{\hbar}{P} = 1/k$ is reduced de Broglie wave length. Clearly the above cross section depends on the energy of the projectile ($E = E_p$) and maximizing at $E_p = E_0$, the central value of the Lorentzian distribution in Figure 2.7. Particles in a stellar environment in thermodynamic equilibrium are distributed according to the Maxwell-Boltzmann velocity distribution $\phi(v)$, given by [15]

$$\phi(v) = 4\pi v^2 \left(\frac{\mu}{2\pi kT}\right)^{3/2} \exp\left(-\frac{\mu v^2}{2kT}\right), \qquad (2.36)$$

where μ is the reduced mass of the projectile and target, k is the Boltzmann constant and T is the stellar temperature. Consequently, the reaction rate per particle pair can be found by integrating the reaction cross section $\sigma(v)$ over phase space, and considering above probability distribution, such that

$$\langle\sigma v\rangle = \int_0^\infty dv \ \sigma(v) \ v \ \phi(v), \qquad (2.37)$$

27

v being the relative velocity between the particles. For non-relativistic particles, we have $E = \frac{\mu v^2}{2}$. Therefore the reaction rate can be rewritten as

$$\langle \sigma v \rangle = \left(\frac{8}{\pi \mu} \right)^{1/2} \frac{1}{(kT)^{3/2}} \int_0^\infty dE \ \sigma(E) \ E \ e^{-E/kT}. \qquad (2.38)$$

Finally plugging in the energy-dependent cross section, the nuclear reaction rate reduce to

$$\langle \sigma v \rangle = \left(\frac{2\pi}{\mu kT} \right)^{3/2} \hbar^2 e^{-E/kT} \omega \gamma, \qquad (2.39)$$

where we define $\gamma = \frac{\Gamma_p \Gamma_\gamma}{\Gamma}$ and have used the fact that $\int_{-\infty}^{\infty} dx \ \frac{a}{(b-x)^2 + a^2} = \pi$.

2.2.2 The $^{31}\text{S}(\text{p}, \gamma)^{32}\text{Cl}$ reaction

From an astrophysical point of view, the $^{31}\text{S}(\text{p}, \gamma)^{32}\text{Cl}$ reaction rate is important as it influences the duration of the Si-P cycle in explosive hydrogen burning environments. In particular, the reaction rate is important to understand the anomalous abundance of sulphur in novae ejecta like the case in Nova Her 1991 [24]. The abundance of other intermediate mass elements such as neon in the Nova Her 1991 spectra reveals the presence of a massive ONeMg white dwarf in a binary system, thereby classifying it as a ONeMg nova [25]. This indicates that the progenitors of the ejecta are mainly oxygen, neon and magnesium. However, the optical spectrum shows a strong sulphur line and this enhancement, shown in Figure 2.9, is still unexplained [24].

According to the present stellar models, the temperature range in ONeMg novae is approximately 0.1 GK $\leq T \leq$ 0.3 GK [26]. In these conditions, the $^{31}\text{S}(p, \gamma)^{32}\text{Cl}$ break out reaction is feasible due to three low-lying resonances in the compound ^{32}Cl nucleus [27], namely at 1738, 2131 and 2209 keV respectively. These are shown in Figure 2.10. Currently there exist discrepancies

28
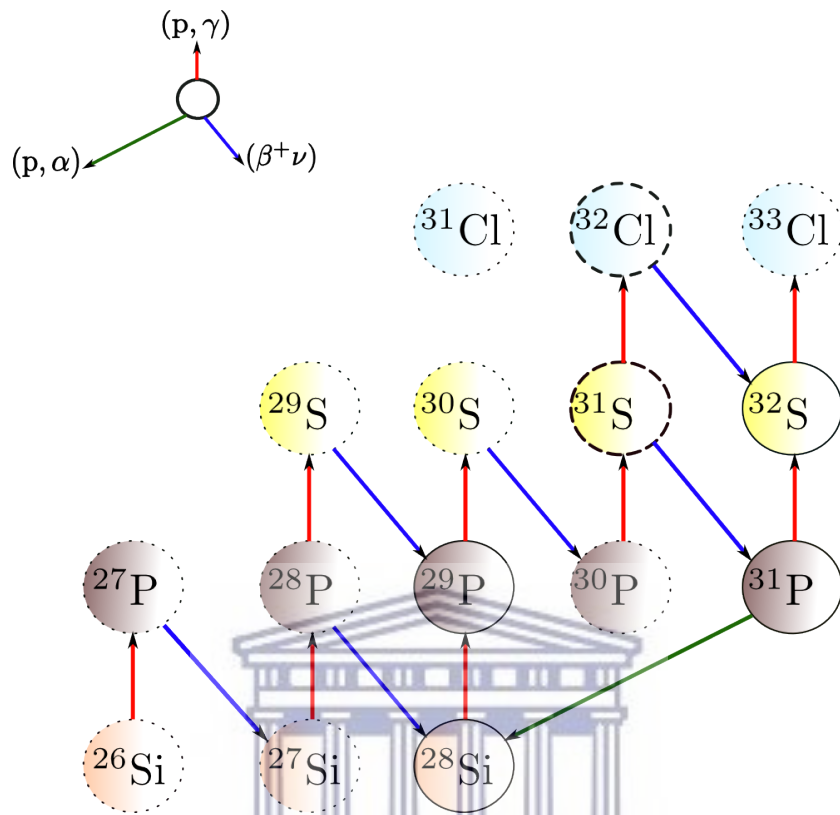
Figure 2.8: Si-P burning cycle.

in the estimation of the reaction rate, which, as shown in Eq (2.39), depends exponentially on the resonance energy. It is therefore natural to expect that these discrepancies are due to differences in past measurements of the resonance parameters. This assumption is validated by recent high precision measurements of the astrophysically relevant excitation energies in ^{32}Cl that have disagreed with one another by close to 3 standard diviations [28, 29]. Recently it was pointed out by Wrede *et al.* [30] that the possible reason for the discrepancy between the two highest precision measurements could be due to potential problems with detection thresholds set by one (that used the Yale split pole spectrograph [28]) compared to to the other (that used the Q3D spectrometer in Munich [29]). This hypothesis was supported by
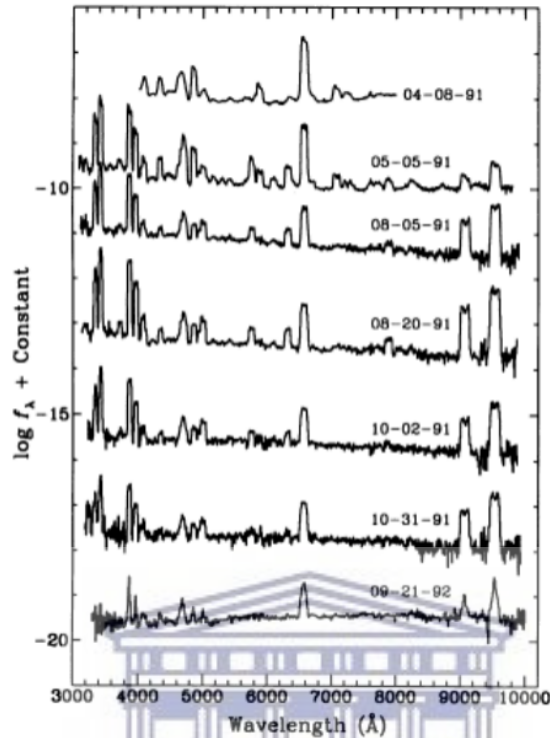
Figure 2.9: Time snapshots of Nova Her 1991 optical spectrum. The sulphur lines with $\lambda = 9069\ \mathring{A}$ are strongly populated during the period from May-October 1991. Figure taken from [24].

an independent measurement of some of the γ-ray energies from transitions in ^{32}Cl, following ^{32}Ar β decay [31]. Most recently, a high-resolution γ spectroscopy experiment was preformed using a Gammasphere array at Argonne National Laboratory [32] to investigate this further and remeasure the resonance energies for all the astrophysically relevant states in ^{32}Cl.

In this work we independently investigate the possibility of remeasuring the energies of the relevant states in ^{32}Cl using the ^{32}S(^{3}He, t)^{32}Cl reaction with the K600 magnetic spectrometer. Additionally, we look into the feasibility of measuring Γ_p, the proton widths of the state of interest using a segmented Si array called CAKE [33]. We also develop a procedure to make other similar future measurements that are relevant for novae nucleosynthesis.

30
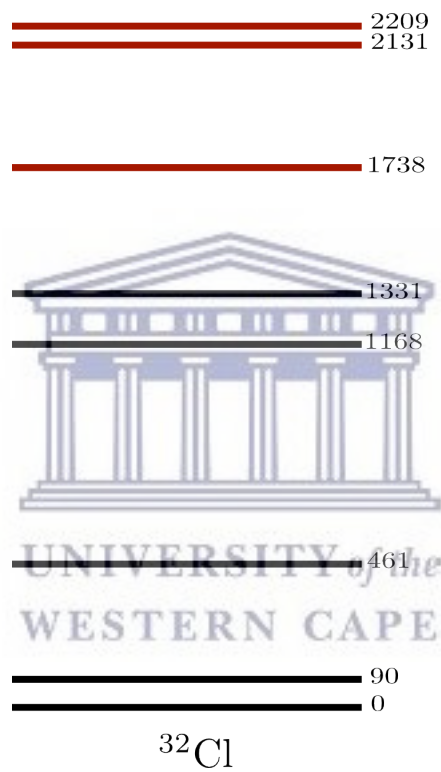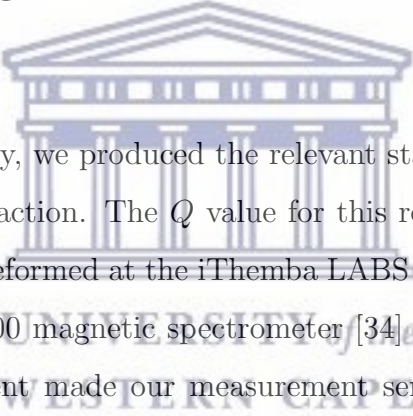
Figure 2.10: Energy levels in ^{32}Cl. The ^{31}S$(p, \gamma)^{32}$Cl break out reaction is feasible due to the resonances marked in red.

31

Chapter 3

Experimental set-up and techniques

As mentioned previously, we produced the relevant states of interest in ^{32}Cl using the ^{32}S(^{3}He, t) reaction. The Q value for this reaction is $\approx$ -13 MeV. The experiment was preformed at the iThemba LABS cyclotron facility with the high resolution K600 magnetic spectrometer [34] operating in 0° mode. This unique arrangement made our measurement sensitive to low angular momentum transfers which was ideal, as we were interested in populating low spin states. Simultaneously, we used a position sensitive silicon detector array called CAKE (Coincidence Array for K600 Experiments) [33] that was located in the scattering chamber and mounted at backward angles with respect to the beam. The main purpose of the CAKE array was to detect unbound protons from excited states in ^{32}Cl.

Our experiment used an incident beam energy of 50 MeV that was delivered to the K600 scattering chamber. A schematic of the K200 separated-sector cyclotron (SSC) facility of iThemba LABS is shown in Figure 3.1. I describe the rest of the experimental set up below.

32
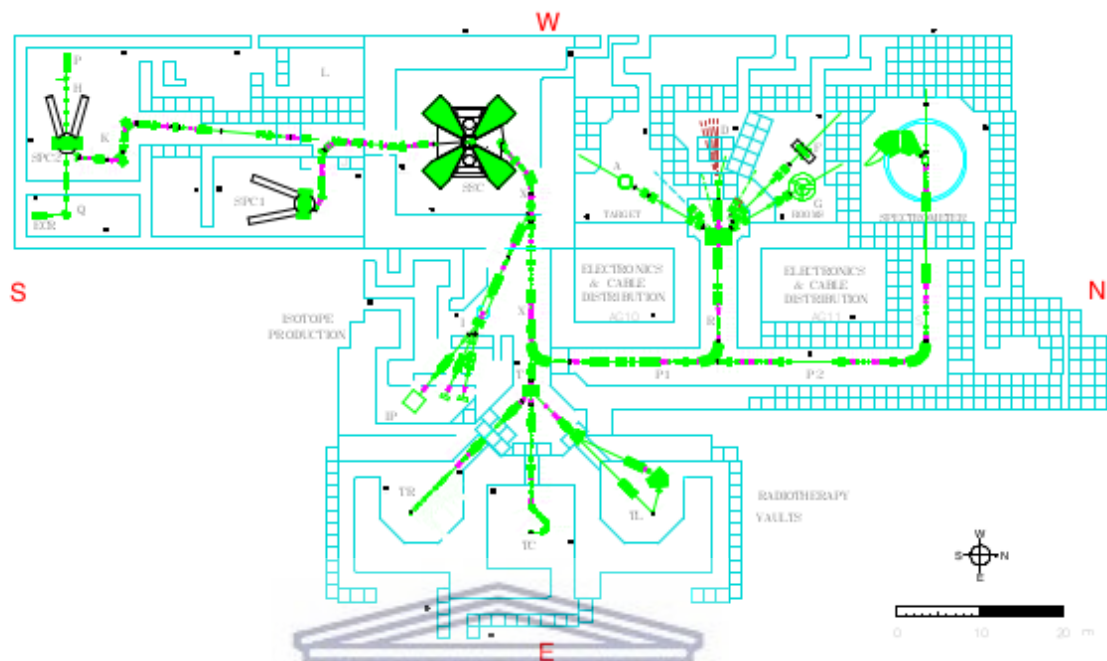
Figure 3.1: SSC facility at iThemba LABS, Figure taken from [35].

3.1 Target preparation

In general, sulphur targets are difficult to make, due to the high vapour pressure and low melting points of elemental sulphur. Due to this property, sulphur targets sublimate is vacuum as they get bombarded by an accelerated ion beam. Therefore, is is preferred that S targets are prepared by depositing a compound on a solid backing [36]. This is done by placing a sulphur compound in a vacuum chamber and thermally evaporating it on the backing, as seen in Figure 3.2. Similarly, enriched S targets can also be made in compound form. For this experiment we made both natural and enriched targets. The latter were made using 99.99% enriched ^{32}S powder, following the method suggested by Watson [37]. In this procedure the ^{32}S powder was placed on a ceramic plate placed ~ 10 mm away from a 300μg/cm^2 Ag foil. The Ag foil was placed at a constant temperature of 150° C. Next the

33

temperature of the Pt boat was raised to $\sim 200°$ C. The sulphur vaporizes at this temperature and form a uniform layer of AgS on the foil. This method has the advantage that the high affinity between silver and sulphur makes the compound formation highly favourable. Also silver is an unreactive metal and hardly reacts with air. We also made ZnS targets with thickness of $\sim 150\mu g/cm^2$, where ZnS material with natural sulphur was evaporated in ^{12}C backing using the thermal deposition method. The chamber used for making the targets is shown in Figure 3.2.

Figure 3.2: Vacuum chamber used for thermal evaporation of ZnS.

3.2 The magnetic spectrometer

 A schematic of the K600 spectrometer is shown in Figure 3.3. It consists of one quadrupole Q and two dipole magnets, D_1 and D_2. The quadrupole focuses the beam vertically and the dipoles are used for momentum dispersion. The K and H trim coils shown in the picture are used to focus the ejectiles at the focal plane [35]. The spectrometer acceptance angle of 3.5 msr is defined by a collimator positioned upstream from the quadrupole.

 Since charged particles enter the spectrometer in a perpendicular direction
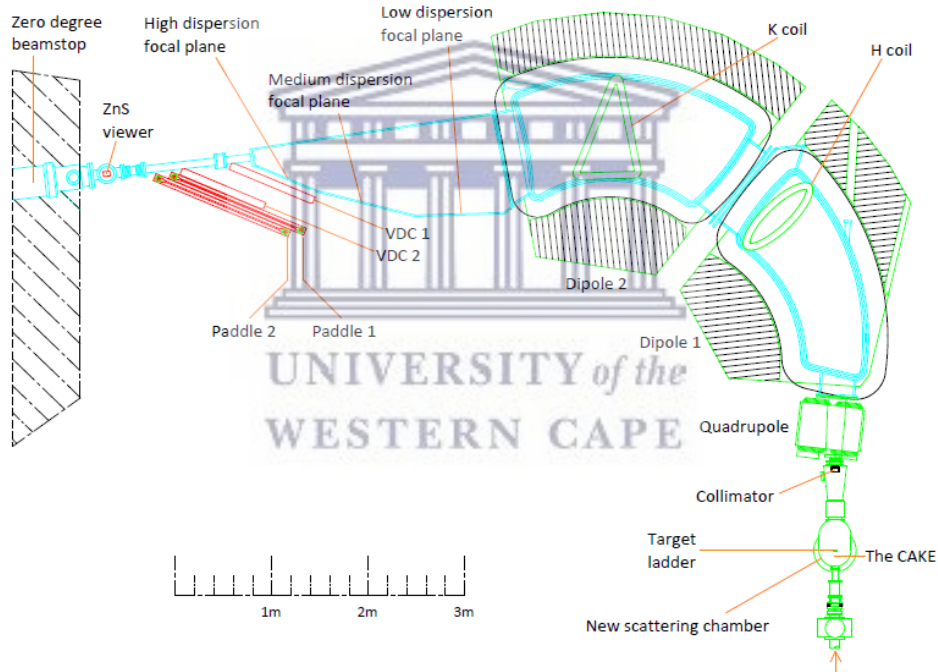
Figure 3.3: K600 spectrometer at iThemba LABS, Figure taken from [35]

to the magnetic field then, it follows that

$$qvB = \frac{mv^2}{r} \implies rB = \frac{p}{q} = \rho, \qquad (3.1)$$

35

where B, is the magnetic field, r is the radius of the curvature of the particles, and we define ρ to be the rigidity, the ratio of momentum to charge for a given ejectile. From Eq. (3.1) it is obvious that the rigidity of a particle is proportional to the radius of curvature in a fixed magnetic field. Therefore, there is a unique radius of curvature associated with the particle's rigidity. Alternatively we can also define an energy constant $K = \frac{2mE}{q^2}$, so that

$$\rho = \sqrt{2K}. \tag{3.2}$$

According to the above equation, two different particles with the same energy constants can have the same rigidity, and consequently hit the same position on the focal plane. However this problem can be solved by particle identification using the time-of-flight (TOF) and energy loss properties to distinguish between particles for different charge and mass. This method is discussed in further detail in the following sections.

In a typical spectrometer experiment, the charged particles exit the second dipole D_2 through a kapton window to a position-sensitive focal plane detector placed at an angle of 35.75° with respect to the beam axis. The distance from the target to the focal plane in roughly 8 m. Since the focal plane detector are mounted on air, the ejectile has to travel through both the kapton window and air before passing through the focal plane. This sets certain restrictions on particle detection energies.

3.3 Focal plane system for the K600

The focal plane detection system for the K600 spectrometer consists of two components (Figure 3.4)

36

- The Vertical Drift Chamber (VDC): To track the particles' trajectory in the focal plane.

- A plastic scintillator, which is used to generate event triggers and for particle identification.
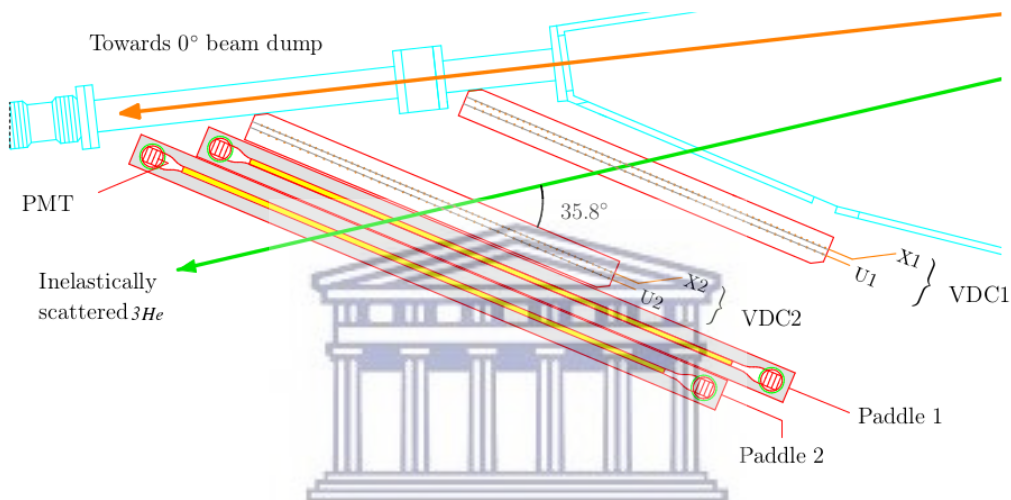
Figure 3.4: Schematic representation of focal plane detector [38]. This picture shows two VDCs and scintillator paddles unlike our set up.

3.3.1 The vertical drift chamber (VDC)

The VDC contains a set of wire planes mounted inside a gaseous medium. It is used to track the trajectories of the ejectiles. When an ejectile traverses the VDC, its ionizes the gas atoms and produces electron-ion pairs. The free electrons start to drift towards the corresponding signal wire and eventually initiate avalanches. The direction of the drift is used to reconstruct the ejectile trajectory; and provide the ejectiles' focal plane position. Together, the focal plane position information and the reaction kinematics calibrate the focal plane spectrum to determine the corresponding recoil's excitation

37

energy. The VDC is made of four components that are described briefly below (see Figure 3.5).
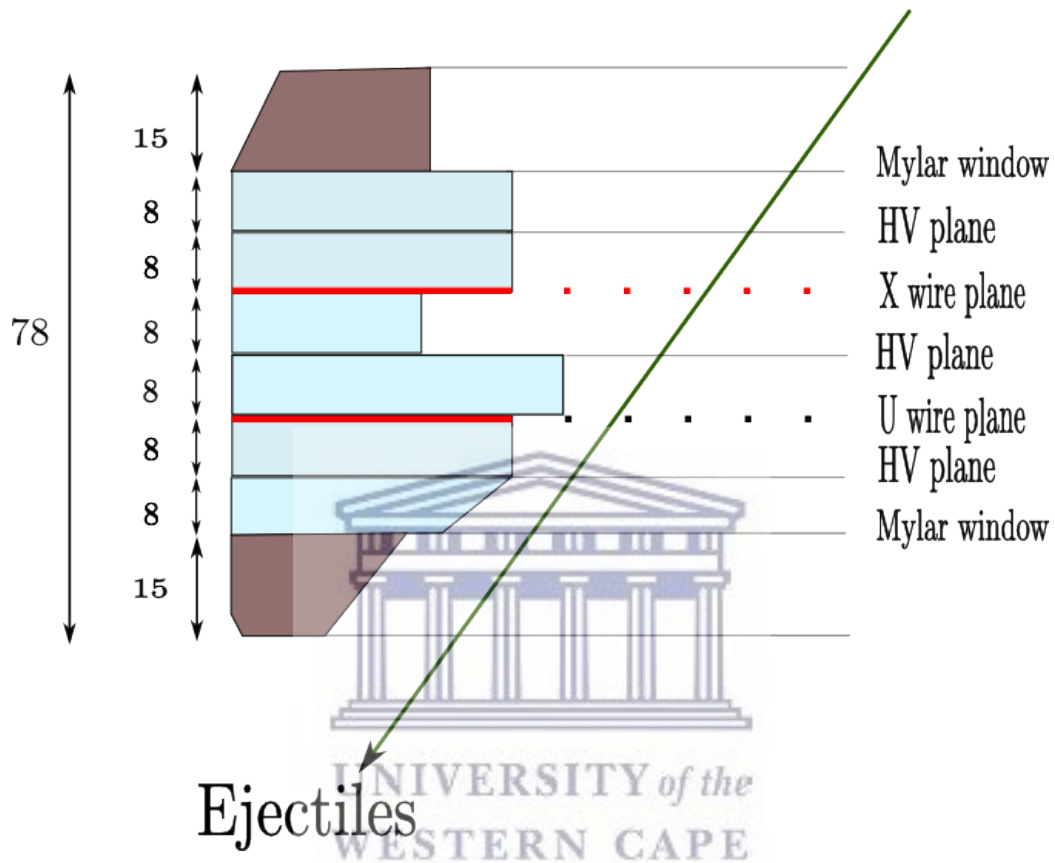
Figure 3.5: VDC top view. The blue part is composed of Stesalam EP107-M950-40 which is a glass fibre and epoxy composite used for isolation. The brown components are composed of aluminium. The wires are mounted inside the red regions which indicate the printed circuit boards (PCB). The dimensions displayed on the left are in millimetres.

Mylar windows

Mylar windows are used to isolate the VDC internal parts from atmosphere and they additionally help in reducing the background. They are made of biaxially-oriented polyethylene terephthalate (BoPET) polymer [35].

High-voltage planes

The VDC contain three high-voltage planes that divide the VDC into X and U wire chambers, as shown in Figure 3.6. The high-voltage planes control the ionization processes that take place in the VDC. For a relatively high potential, the VDC operates in the Geiger-Müller mode, while at lower voltages, it operates in ordinary ionization mode. In the ordinary ionization mode, the freed electrons themselves trigger the signal wire. However, in the Geiger-Müller mode, because of the relatively high voltage applied, the accelerated electrons collides with other gas atoms and liberate more electrons. The newly ionized electrons are also accelerated, this leads eventually to an electric cascade called the Townsend avalanche [39]. This effect prevents us from accurately deducing the energy deposited by the ejectiles since the collected signal results from several electron cascades. However, this regime can be useful for the case of detecting low energy ejectiles. Therefore, in our experiment the VDC was operated in ordinary ionization mode, with the high voltage set at -3.56 keV.

The wire planes

The X and U wire planes are placed inside the gas chamber. The X wire plane consist of 198 signal wires and 201 guard wires. The U wire plane on the other hand consists of 143 signal wires and 146 guard wires [35]. All wires are made of gold plated tungsten. These wires serve the following functions:

- The signal wires create an electric field gradient to drift the ionized electrons towards them. This leads to avalanching close to the signal wire. The wires are connected to pre-amplifiers which then pass the signals to Time to Digital Converter (TDC) modules of the K600 data acquisition system.

39
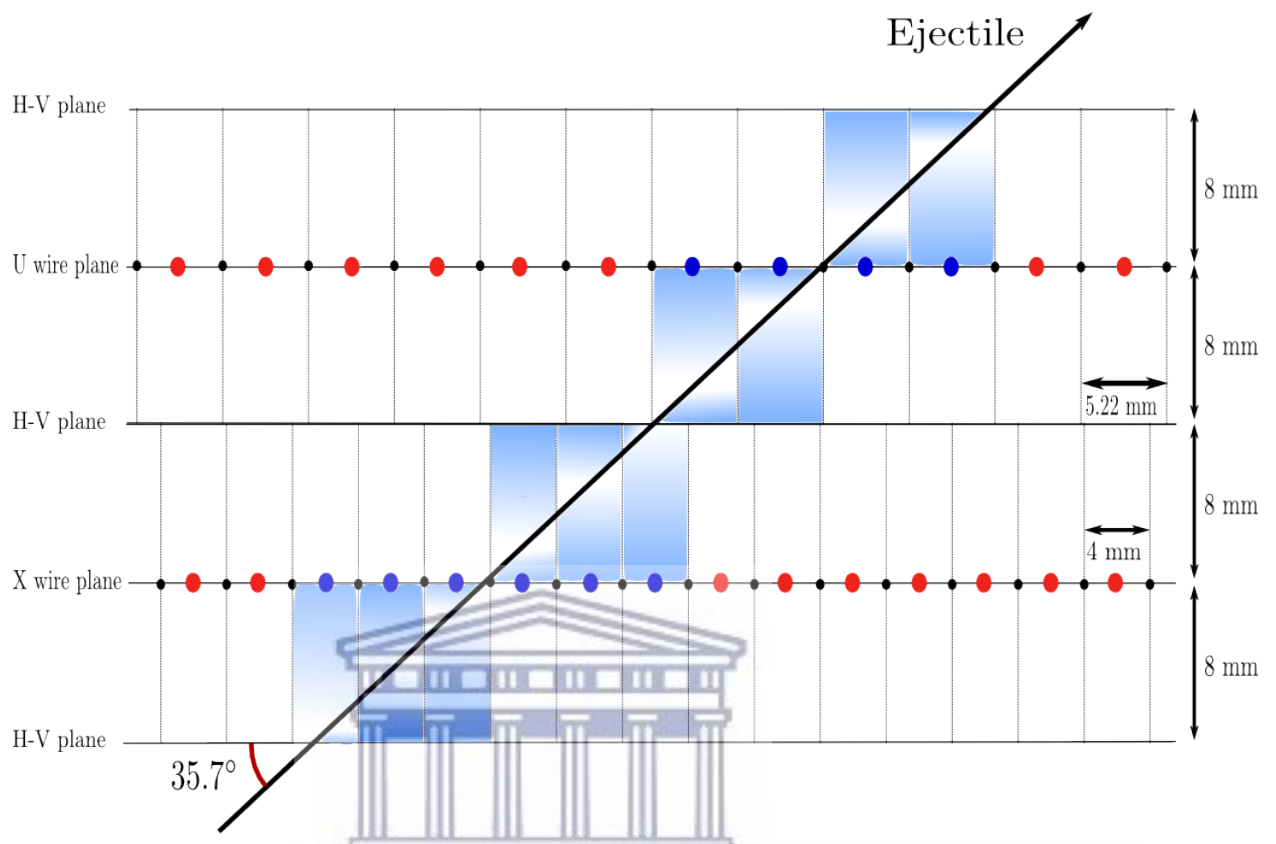
Figure 3.6: VDC top view. The signal wires are represented by red and blue circles. The blue ones correspond to wires within active cells. The guard wires represented by black dots. The bluish gradient in the active cells is to mimic the electron avalanches near the signal wires.

- The guard wires are evenly interspersed amongst the signal wires. They are set at a voltage of roughly 500 V. This configuration creates an active cell for each signal wire. The active cell border defined by the guard wires potential together with the high voltage planes potential is shown in Figure 3.6. This configuration also prevents the electrons from the cross-cell drifting.

The X wires are mounted vertically to the horizontal plane, to gives horizontal position information about the ejectile. The U wires are tilted at 50° to the horizontal plane and give both vertical and horizontal information.

40

The gaseous medium

The gaseous medium of the VDC is filled with 90% Ar gas and 10% of CO_2 which works as a quenching gas. The latter is used because sometimes the energy deposited by the traversed particle is not enough to ionize gas atoms. Such a situation would rather excite the atom, which eventually de-excites and emits photons, which in turn could liberate electrons in a different positions resulting in a fake signal. The CO_2 quenches the phenomenon by absorbing the photon energy.

VDC operating mechanism

Ionized electrons inside the VDC's wire planes drift toward the signal wires to create avalanches in their vicinity and eventually induce electrical signals. The signal generated is processed by pre-amplifiers and passed to the Data Acquisition System (DAQ). The ejectiles' positions are inferred by measuring the average drift times of the electrons with respect to the triggering times of the scintillator paddles. This information is used to obtain the average drift distance covered by the ionized electrons towards the signal wires. In this configuration of the VDC's wire planes, the maximum distance between any of the high voltage plane to the wire plane is 8 mm.

3.3.2 Plastic scintillator

A plastic scintillator paddle was used to trigger the DAQ and to generate particle identification spectra. It is made of BC-408 plastic scintillator material and wrapped in aluminised mylar [40]. The paddle is connected to two photomultiplier tubes (PMTs), mounted vertically at both ends. The scintillation signals were amplified by the PMTs, and further passed to the

41

Figure 3.7: Plastic scintillators at the K600.

DAQ. This scintillator was also used for particle identification (PID), using the TOF, which is the time between the radio frequency of the cyclotron (RF) and the event trigger time at the paddle. This PID procedure is a highly sensitive method to gate on the ejectile channel, it can separate different particles with equal rigidities and even subtract background.

3.4 Coincidence Array for K600 (CAKE)

The coincidence array for K600 (CAKE) shown in Figure 3.8, is composed of five MMM-type double-sided strip silicon detectors (DSSSD). It was manufactured by Micron Semiconductor Ltd[33], for use with the K600 spectrometer to allow detection of charged particles ejected by the recoiling nuclei in

42

the scattering chamber. CAKE is mounted at backward angles to minimize the risk of radiation damage. CAKE, is positioned to cover angles ranging from 115° to 165° with respect to the beam axis, yielding a total efficiency of 25% coverage of the solid angle. The p-side of the MMM-type DSSSD is composed of 16 rings while the n-side is divided into 8 sectors, as seen in Figure 3.9.
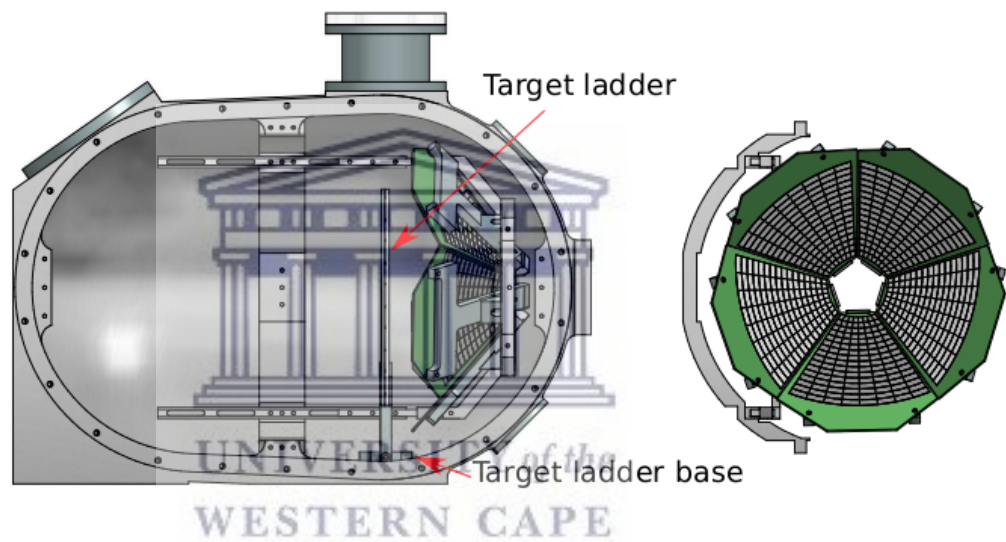
Figure 3.8: (Left) The scattering chamber with CAKE mounted at backward angels while the beam enters from the right direction. (Right) CAKE geometry, Figure is taken from [33].

43
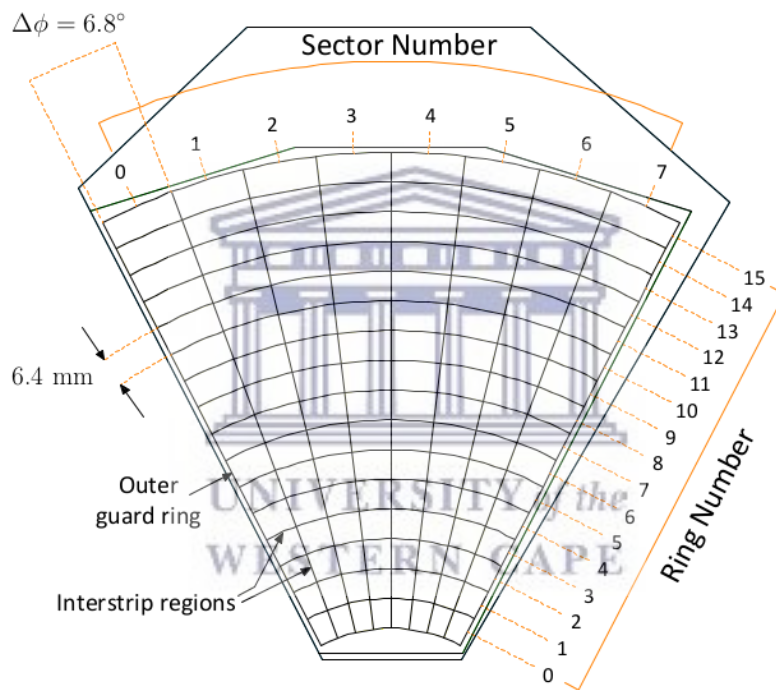
Figure 3.9: A schematic of the DSSSD.

Chapter 4

Analysis

For the experiment we collected ~ 44 hours of ^{32}S(^{3}He, t) data using both the focal plane detectors and CAKE, with the K600 data acquisition system. These data were analysed using the ROOT software. I describe the analysis procedure below.
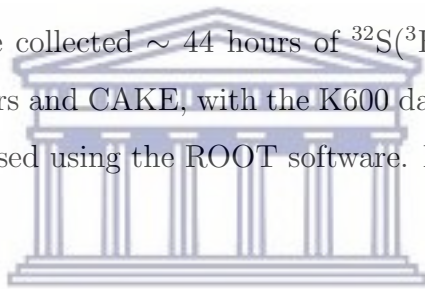
4.1   CAKE energy calibration

Prior to the experiment, a ^{228}Th calibration source was used for calibrating the CAKE array. This is because the decay of ^{228}Th yields well defined α-peaks from the decay chain as shown in Figure 4.1. Figure 4.2 shows the ADC signals collected with CAKE and the ^{228}Th source mounted on the target frame of the K600 scattering chamber. As evident in Figure 4.1, one would expect at least 6 intense α peaks in the CAKE spectrum, for each individual strip, within the energy range 5.2 MeV $\leq$ E$_\alpha$ $\leq$ 8.7 MeV. Some of these peaks would be closely spaced to one another (appear as doublets). However these would be difficult to identify, considering the energy resolution of the Si detectors, which have a full width of half maximum (FWHM) $\approx$ 100 keV as

45
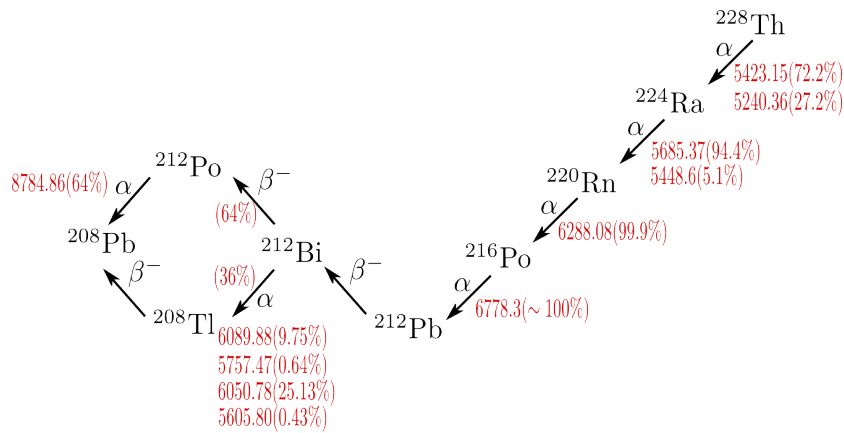
Figure 4.1: The ^{228}Th decay chain.

shown in Table 4.1. In such a scenario it is not unreasonable to fit a doublet as one individual wide peak, with the FWHM as a free parameter.

Our first step for the energy calibration of CAKE was to fit the individual α spectra in each of the 120 strips (8 sectors and 16 rings for 5 DSSSDs) for the CAKE array. This was preformed using pure Gaussians as fit functions on a flat background. The peak centroids, FWHM and peak areas were free parameters. The energy calibration for each of these 120 spectra were preformed using the coefficients of a linear regression

$$E(i) = a_i + b_i(X_i), \tag{4.1}$$

where the X_i are the peak centroids, and a_i and b_i are the offsets and the gains respectively. This calibration procedure allowed us to add gain-matched signals from each of the 120 channels into a summed CAKE spectrum. This is highlighted in Figure 4.2, which shows an uncalibrated 2 dimensional spectra from CAKE, obtained using 12-bit CAEN ADCs (4096 channels on the horizontal axis). The 5 DSSSDs in the array are grouped in such a manner that each horizontal band in the 2D histogram corresponds to 24 channels from

46
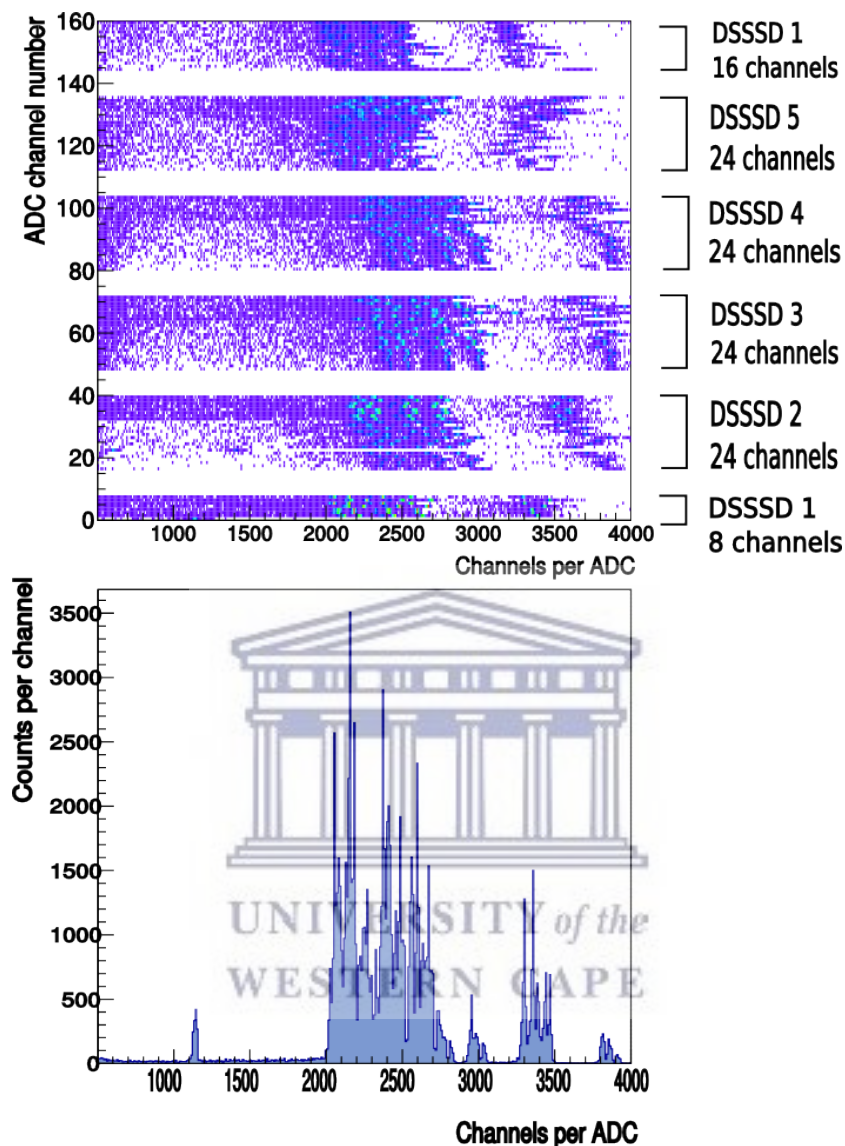
Figure 4.2: Top panel: Representation of uncalibrated ADC signals from CAKE. Each channel in the figure corresponds to one of CAKE's 80 rings (p-side) and 40 sectors (n-side). Bottom panel: Projected (uncalibrated) ADC spectrum.

each detector (for 8 sectors and 16 rings). The first DSSSD is divided into two groups of 8 + 16 ADC channels as shown in Figure 4.2. The results of the gain-matching are apparent in Figure 4.3, where clearly distinct α-peaks

47
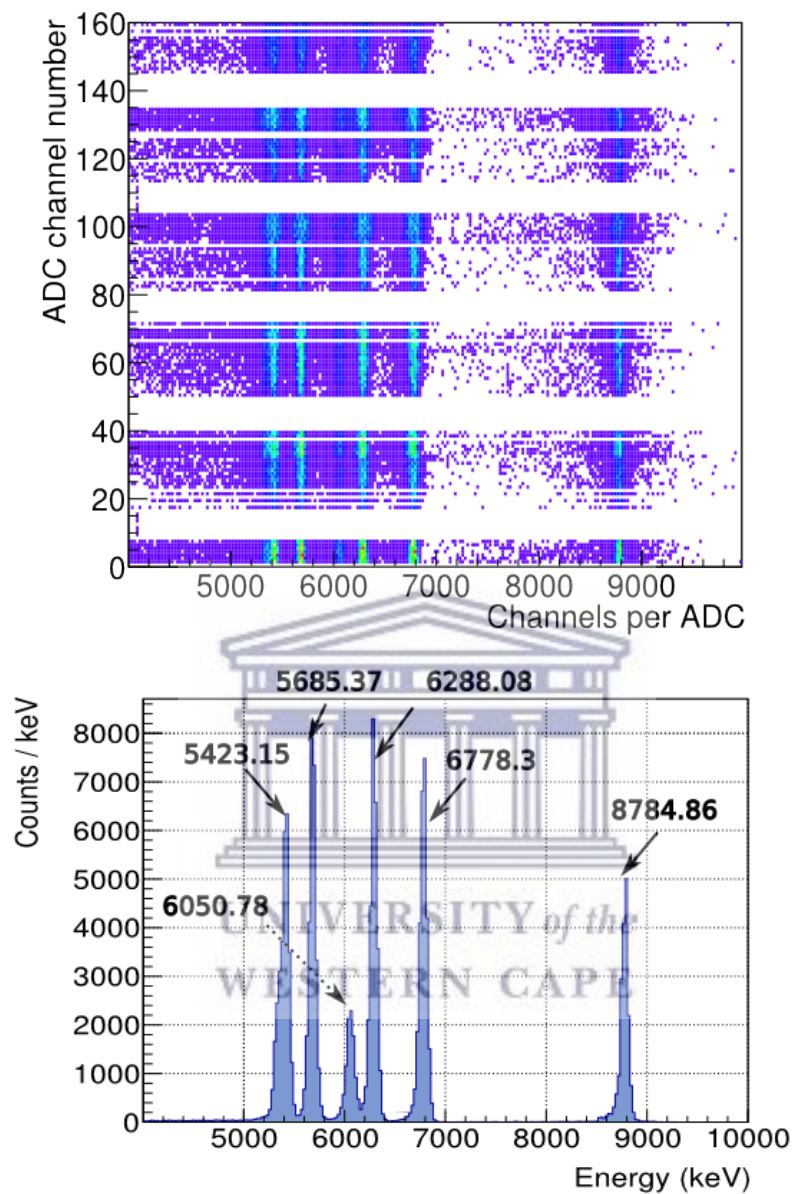
Figure 4.3: Calibrated α spectrum with CAKE.

from Figure 4.1 are identified in the lower panel. Finally, since we expect to detect low energy protons with CAKE, thresholds for the DSSSDs adjusted to the lowest possible values above the noise. The energy resolution achieved in the gain matched α spectrum from CAKE is shown in the table below.

48

Table 4.1: The FWHM's of α peaks that measured by the DSSSDs.

E_α (keV)	FWHM (keV)
5423	121
5685	93
6051	116
6288	93
6778	99
8788	100

4.2 Particle identification (PID) and focal plane calibration

The focal plane singles spectrum is affected by factors such as the quality of the beam, contamination in the target(s), beam induced background and the multiple scattering of the charged light ejectiles. Since the ^{3}He beam induces several other reactions such as $(^3\text{He}, d)$, in addition to the $(^3\text{He}, t)$ reactions of interest, other ejectiles with same rigidity will be detected at the focal plane. To avoid such contamination, the scintillator paddle at the focal plane was used to identify the tritons, in order to obtain a clean spectrum corresponding to ^{32}Cl excited states. To achieve this, we used the energy deposited in the paddle and the time of flight (TOF) of the ejectiles for particle identification. The TOF can be estimated by calculating the flight time of the ejectile from the target to the paddle, so that

$$\text{TOF} = \frac{d}{v}, \tag{4.2}$$

where d is the flight distance within the spectrometer (which varies from 7.78 m to 8.87 m in the medium dispersion mode). The relativistic velocity

49

v in Eq. (4.2) is simply

$$v = c\sqrt{1 - \left(\frac{m}{E}\right)^2}, \tag{4.3}$$

where m and E are the mass and the energy of the ejectile.

This was obtained using the trigger signal from the paddle which was fed into a time-to-digital converter module (TDC) and used as a time reference. Simultaneously, the RF time signal from the cyclotron was also registered with the TDC. The time difference between the RF signal and trigger from paddle provided a relative measurement of the ejectiles' time of flight. From the reaction kinematics (described in the next section), we estimate the kinetic energy of the tritons to range between 31 MeV to 36 MeV. Thus, using the energy deposited on the paddle and the relative TOF, we can identify the triton and the deuteron groups shown in the right panel of Figure 4.4, that arise from $(^3\text{He}, t)$ and $(^3\text{He}, d)$ reactions respectively. Before generating the final spectrum by gating on the triton group, it is also imperative to have an understanding of the beam induced background on the PID spectrum. This is obtained using an empty frame (with no target), whose PID spectrum is shown in Figure 4.4. Since there was a considerable background continuum in our region of interest of the PID spectrum, we added another 2 dimensional gate on the energy deposited at the paddle as a function of the focal plane position, shown in Figure 4.5. The application of this additional gate ensured a more stringent selection of triton events, as shown in Figure 4.6. The effect of the application of these PID gates on the focal plane position vs TOF spectrum is illustrated in Figure 4.7.

50
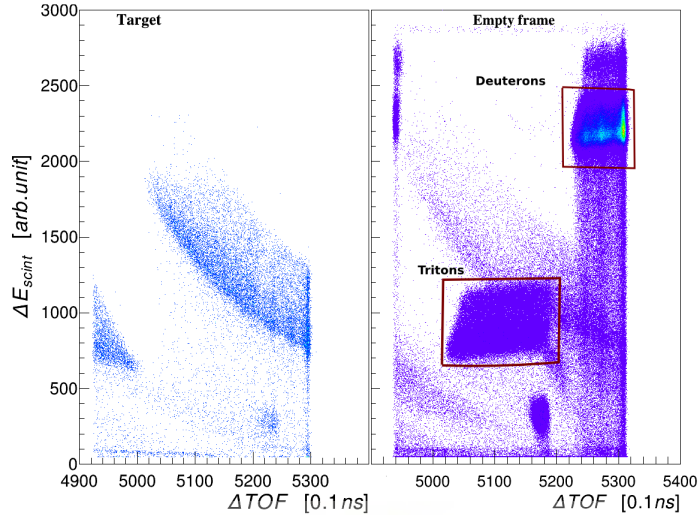
Figure 4.4: Energy deposited at the paddle as a function of relative time-of-flight (TOF). Left panel: Focal plane events corresponding to an empty target frame. Right panel: Focal plane events collected using a AgS target.

4.2.1 Focal plane energy calibration

We performed an internal energy calibration for the focal plane using known excited levels in ^{32}Cl [41]. In order to do that, we first started with a rough calibration so that we could correctly identify the peaks of interest. For this we used a relativistic kinematics code (called SPANC), which was developed by the Wright Nuclear Structure Laboratory at Yale University [42]. As shown in Figure 4.8, SPANC estimates the relative focal plane positions for different ejectiles from various nuclear reactions, based on their rigidity. Additionally, this code is also useful to identify potential contaminants from reactions on the backing material and other impurities in the target. For example, in this experiment we used a silver foil as a backing in one target and for the second we had ZnS compound evaporated on a carbon backing. Furthermore, as also seen in Figure 4.9, the SPANC predictions show that we expect to see some contamination from oxygen impurities in the target,

51
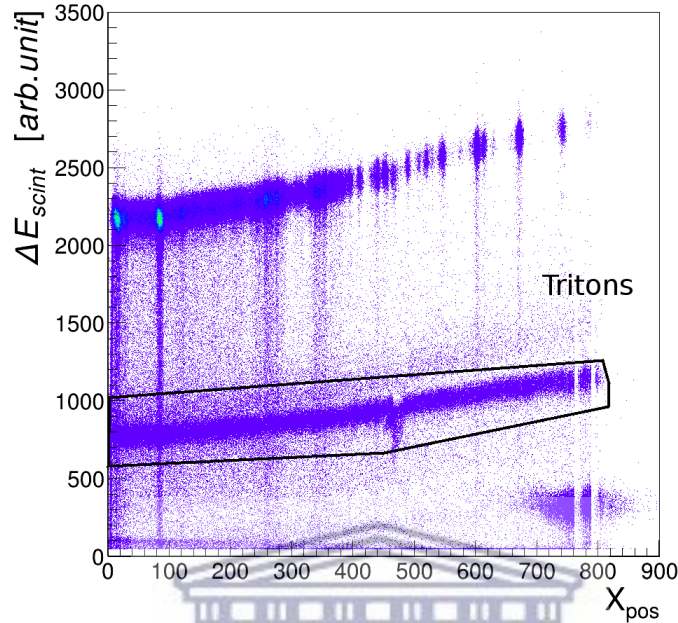
Figure 4.5: Paddles' energy as a function of the focal plane positions, the lower band represents triton events. This is because the Q value for the $(^3\text{He}, t)$ reaction is much more negative than $^{32}\text{S}(^3\text{He}, d)$ reaction.

corresponding to 424 keV and 721 keV excitations in ^{16}F. Also, tritons corresponding to the ^{12}N ground state also fall in the region of interest. This is highlighted in Figure 4.10, which shows that the ^{12}N ground state is strongly populated with the ZnS target, due to reactions on the ^{12}C backing material.

After confirming the excitation energies above, we are in a position to perform an internal calibration. The calibration procedure is explained below. Since the K600 is essentially a momentum spectrograph, it is more accurate to perform the calibration using the ejectile momenta P_t, rather than ejectile energies. In order to achieve this we used a relativistic kinematics code to reconstruct the ejectile momenta $P_t(i)$ using the known excitation energies $E_x(i)$ of the recoiling ^{32}Cl* nuclei. Next, we calculated $P'_t(i)$, which are the triton momenta corresponding to a 1σ shift in the known energies,

52
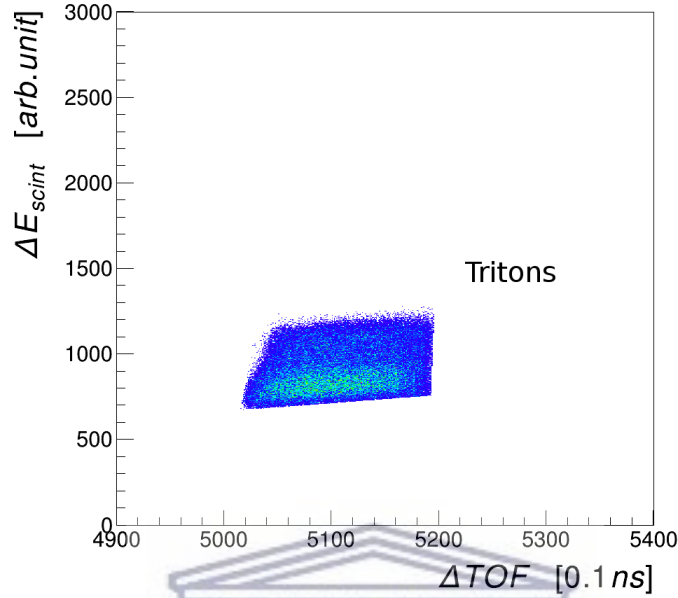
Figure 4.6: Paddle energy as a function of TOF after the PID gate on tritons is applied.

with $E'_x = E_x + \Delta E_x$. The intrinsic statistical uncertainties $\Delta P_t(i)$ is then determined from the absolute value of the difference between these numbers, $\Delta P_t(i) = |(P_t(i) - P'_t(i)|$. These triton momenta were used together with focal plane positions to extract calibration coefficients. For this, we first obtained the centroids of each peak in the focal plane spectrum. These were obtained using a Levenberg Marquardt χ^2 minimization routine, that used a lineshape function which was a convolution of a Gaussian with low energy exponential tails, on flat background [43]. The resulting fits for the relevant ^{32}Cl peaks are shown in Figure 4.11 and listed in Table 4.2.

The extracted peak centroids and their corresponding momenta are finally used to obtain an energy calibration using the quadratic regression

$$P(i) = a_0 + a_1 x_{pos}(i) + a_2 x_{pos}^2(i). \tag{4.4}$$
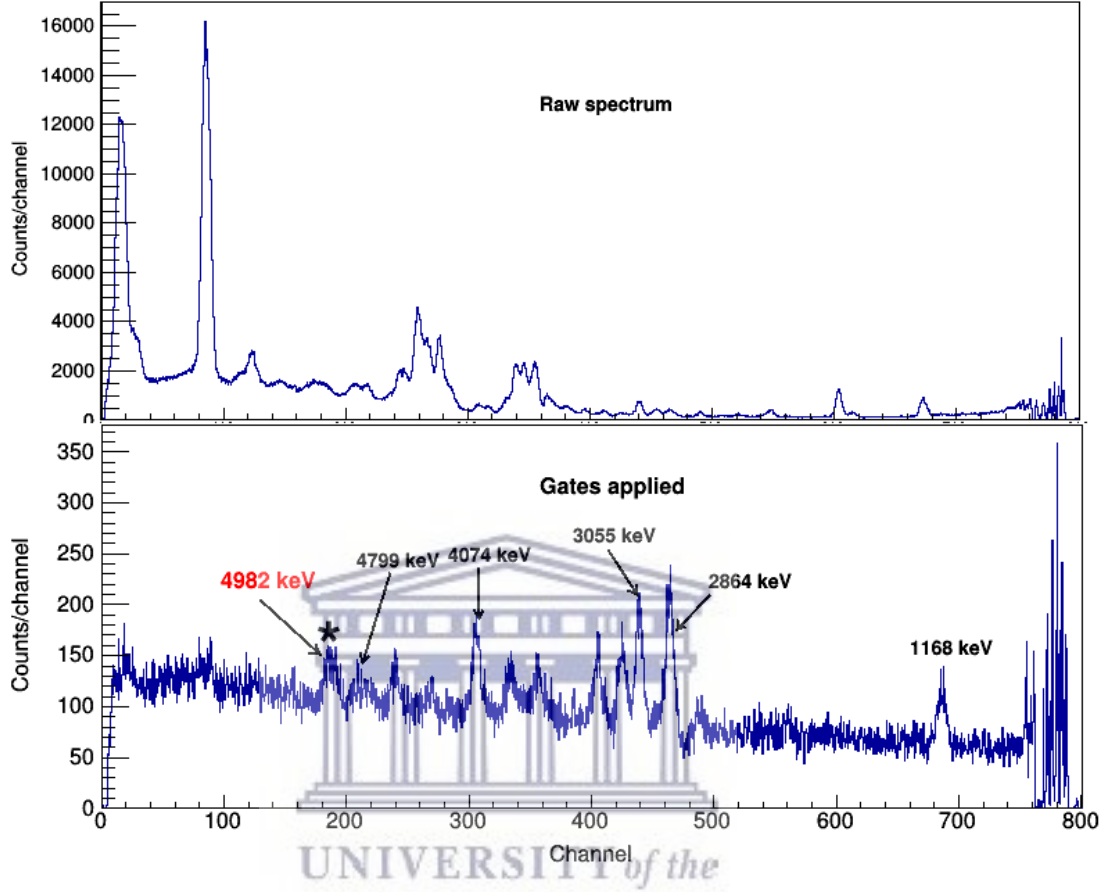
Figure 4.7: Top panel: Raw focal plane spectrum from AgS target. Bottom panel: Triton spectrum generated with the correct PID gates. The peak marked by an asterisk is a potential source of isospin mixing to the $T = 2$ IAS leading to the violation of the IMME.

To obtain the above coefficients and their associated errors, a chi squared minimization was performed with respect to each parameter using $\frac{\partial \chi^2}{\partial a_j} = 0$ where $j = 0, 1, 2$. For this we used a fitting routine within ROOT that employs the effective variance method. Using this method, the chi squared for each data point $P_t(i)$ value is defined as [44]

$$\chi^2 = \frac{P_t(i) - P(i)}{\Delta P_t^2(i) + (\Delta x_{pos}(i) \partial_x P(i))^2} \quad . \tag{4.5}$$

54
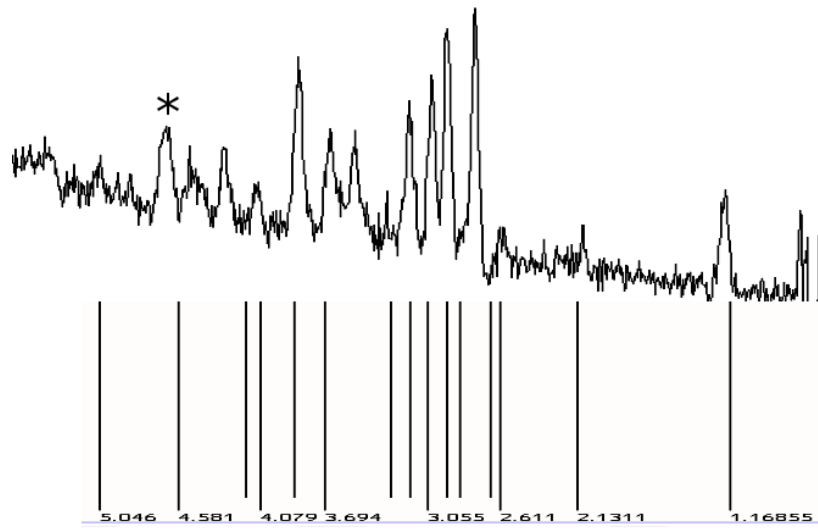
Figure 4.8: Rough calibration for the triton focal plane spectrum using SPANC. All energy units are in MeV.
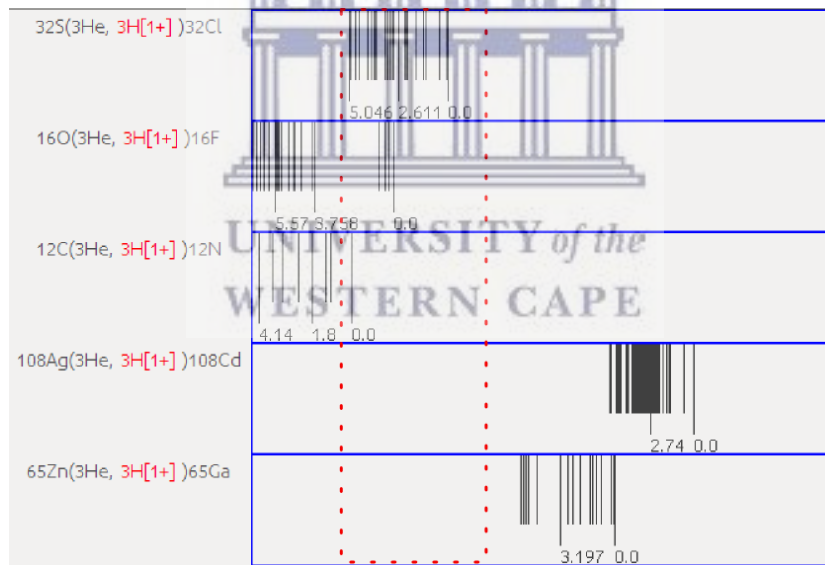
Figure 4.9: SPANC output: The first group represents the focal plane positions of tritons corresponding to ^{32}Cl excitations. Relative focal plane positions for tritons from different nuclear reactions are illustrated in the other levels. The dashed area illustrates the focal plane region of interest for this work. The other reactions are shown due to the possibility of their presence as contaminations in the targets. All energy units are in MeV.

55
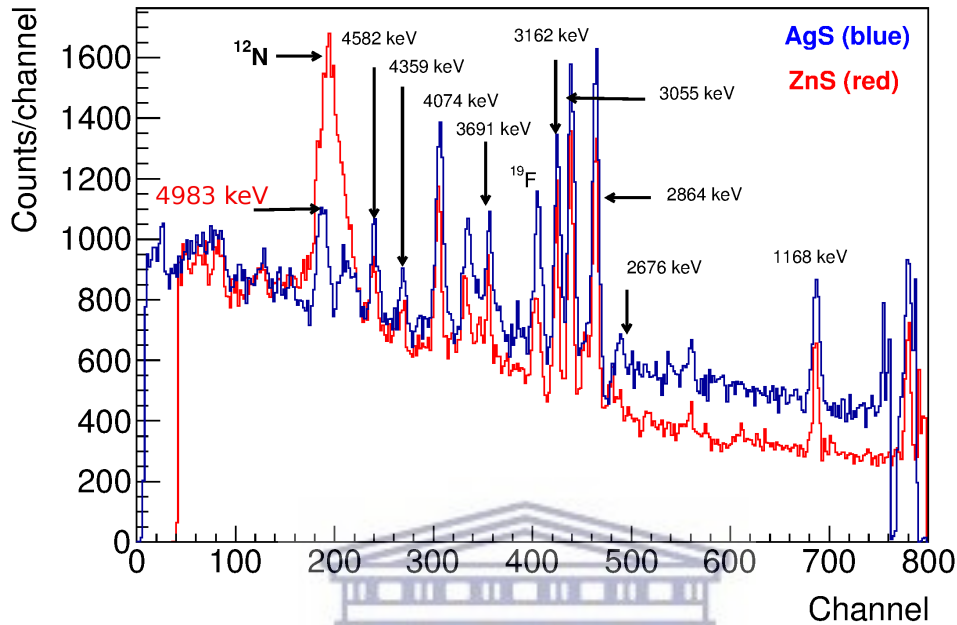
Figure 4.10: Comparison of triton spectra obtained from the two targets. In the ZnS spectrum that is shown in red, the ^{12}N ground state is strongly populated as expected.

The routine starts with initial guesses for the parameters and searches for a χ^2 minimum for a given parameter. The procedure is then repeated for each parameter, until a stable minimum for the χ^2 value is obtained, yielding the coefficients a_j and their associated uncertainties $\Delta^2_{coeff}(j) = \sqrt{\sum_j a_j^2 + cov(j)}$, where $cov(j)$ are the covariances.

Therefore, the uncertainty in the momentum of an unknown peak with centroid X_{pos} is simply

$$\Delta P = \sqrt{\left(\frac{\partial P}{\partial x_{pos}}\right)^2 \Delta x_{pos}^2}, \qquad (4.6)$$

which yields

$$\Delta P = \sqrt{(a_1 + 2a_2 x_{pos})^2 \Delta x_{pos}^2}. \qquad (4.7)$$

56
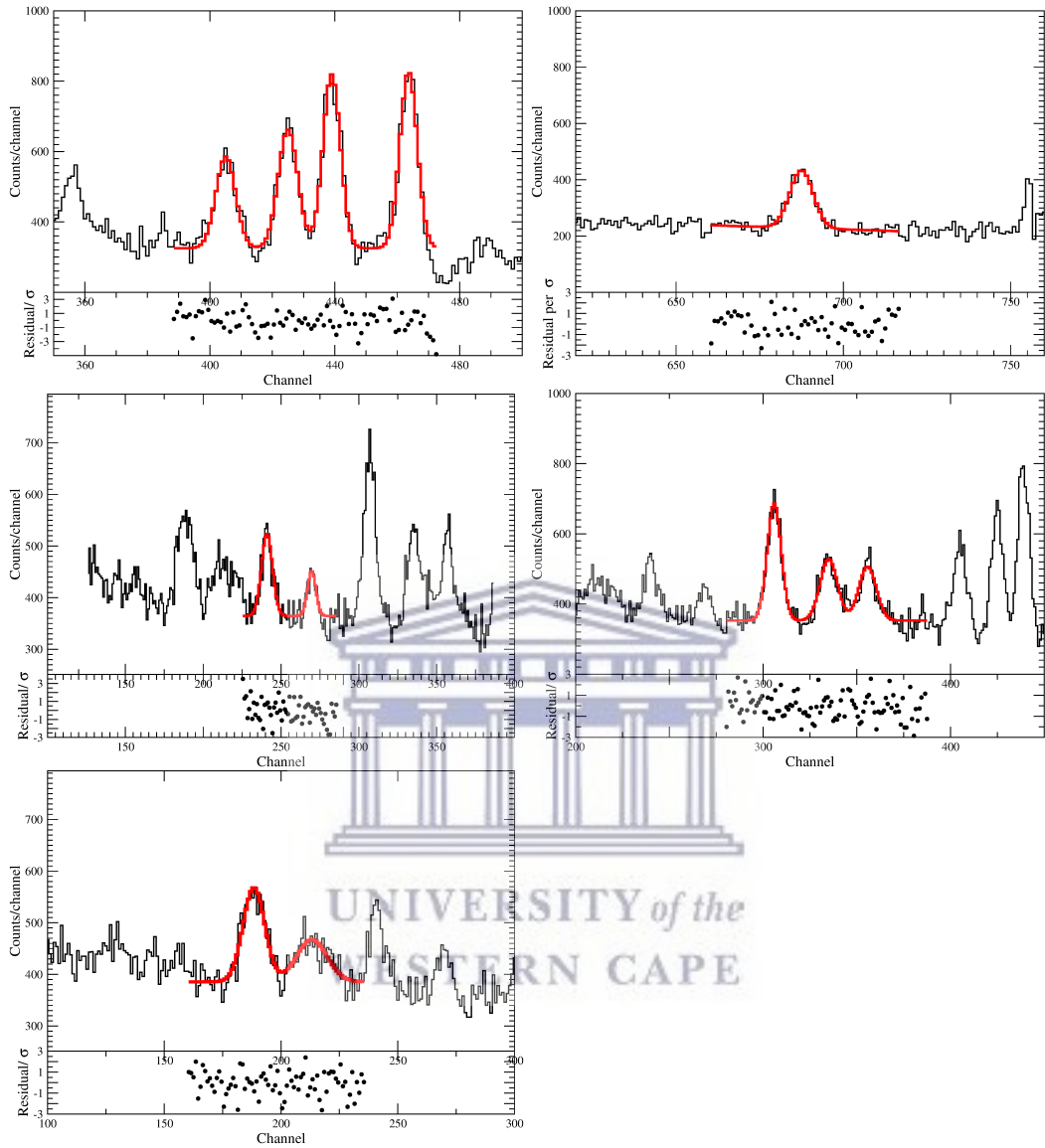
Figure 4.11: Fitting of the tritons focal plane centroids.

The total uncertainty, including the uncertainty contributions due to a_j is then

$$\Delta P_t = \sqrt{\Delta P^2 + \Delta_{coeff}^2}. \tag{4.8}$$

The above procedure allows us to extract the values of unknown excitation energies within the region of interest, by plugging the triton momentum

57

Table 4.2: Experimental excitation energies, ejectile momenta and triton peak centroids for the ^{32}S(^{3}He, t) spectrum at the focal plane (with the AgS target).

E_{exp} (keV)	x_{pos} (mm)	Δx_{pos} (mm)	P_t (MeV)	ΔP_t (MeV)
1168.55 (13)	686.92	0.16	451.29	0.01
2859 (4)	464.49	0.08	440.30	0.02
3055 (5)	439.50	0.09	439.01	0.03
3165 (4)	425.55	0.12	438.28	0.02
3694 (4)	356.48	0.23	434.76	0.03
4079 (4)	306.44	0.14	432.18	0.03
4352 (5)	269.27	0.34	430.34	0.03
4581 (6)	240.26	0.26	428.79	0.04

values for unknown peaks (obtained from the fit) back into the kinematics code. The resulting excitation energies for all identified peaks are listed in Table 4.3 and shown in Figure 4.12. The singles data clearly shows a

Table 4.3: Experimentally determined values of the ^{32}Cl excitation energy values obtained from the calibration fit. Note that the observed state in the last line is not reported in the literature [41]. This is a potential source of isospin mixing as described later in this thesis.

E_{exp} (keV)	E_{fit} (keV)	ΔE_{fit}	Residuals
1168.55 (13)	1168.48	1.25	0.06
2675 (5)	2676.90	3.88	0.38
2131.1 (0.4)	2130.42	2.55	0.26
2859 (4)	2864.34	0.62	8.61
3055 (5)	3055.50	0.66	0.10
3165 (4)	3162.14	0.90	3.17
3694 (4)	3691.06	1.80	0.73
4079 (4)	4074.58	1.08	1.10
4352 (5)	4359.60	2.60	1.52
4581 (6)	4582.15	1.97	0.19
4796 (10)	4799.20	6.83	0.32
?	4982.92	2.02	?

previously unknown peak corresponding to an $E_x = 4983(3)$ keV that is not

58
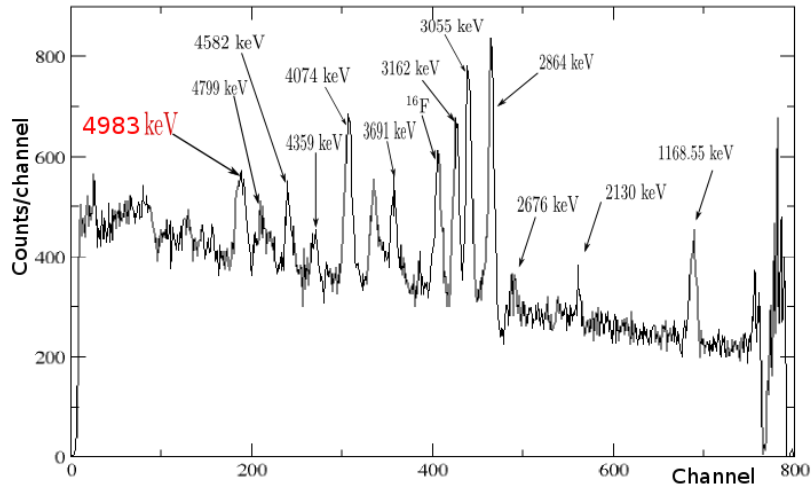
Figure 4.12: Labeled focal plane spectrum with both known and unknown excitation states in ^{32}Cl nucleus. Note the peak at 4983 keV, is $\sim$ 63 keV below the $T = 2$ IAS in ^{32}Cl. This is potentially the source for isospin admixture that cause the IMME violation.

listed on the ENSDF database [45]. It is highly likely that this is the source of isospin mixing that could contribute to the IMME violation for the $A = 32$, $T = 2$ quintet. Unfortunately the ZnS target shows a large contaminant peak from ^{12}C(^{3}He, t) in this region of interest, which makes identifying this 4983(3) keV peak impossible from the singles spectrum. However, since the ground state in ^{12}N is bound, this background is easily removed from triton-proton coincidence described below.

We can identify the tritons that are associated with proton decay events detected in CAKE. This is done by generating a 2D-histogram of the focal plane events versus the energy deposited on CAKE, and applying a gate on the proton groups shown in the top panel of Figure 4.13. Since the triggers are from the paddle detector, the application of this gate projects the tritons in the focal plane spectrum that correspond to only valid charged particle events in CAKE. An overlay of the CAKE-coincidence and singles focal plane

59

spectra is also shown in Figure 4.13. In principle the proton branching ratios and angular distribution can be obtained from these coincidence data, so that one can obtain the ^{31}S(p, γ) reaction rate as well, in addition to affirming the spin and parity of the isospin admixed state at 4983 keV. More detailed explanation is presented in sections 4.4 and 4.5.
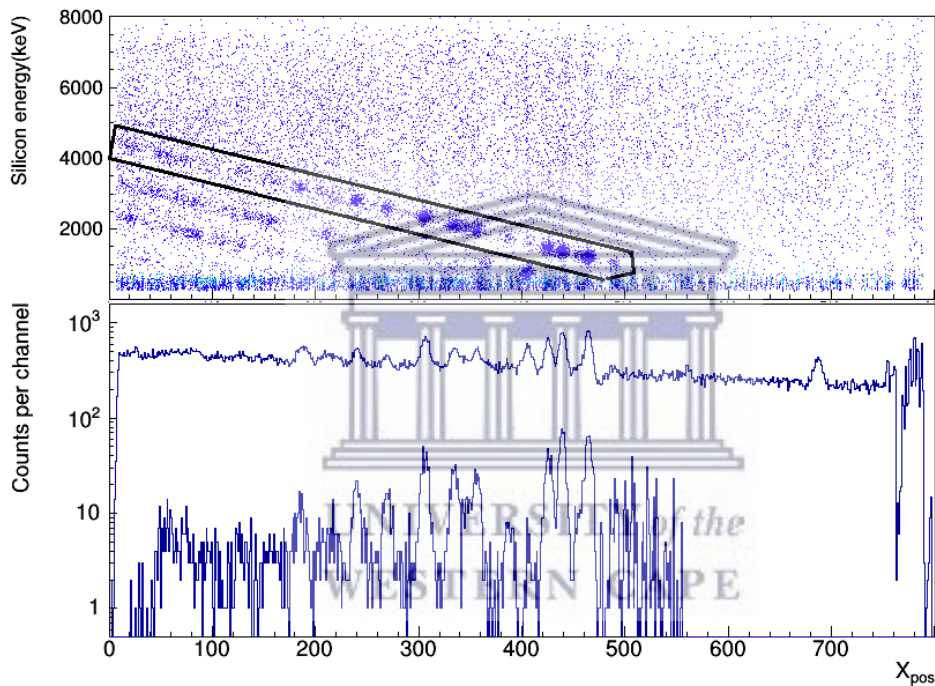
Figure 4.13: Top panel: A 2D-histogram of CAKE energy vs the focal plane position. The marked diagonal in the 2D-histogram highlights proton groups which are used to generate coincidence events. Bottom panel: The upper spectrum is the singles spectrum and the lower one is the proton coincident focal plane spectrum.

4.2.2 Other systematic effects

The K600 spectrometer operating in $0°$ mode has an angular acceptance range of $-2°$ to $2°$ in the laboratory frame. This could affect the resolution

at the focal plane due to differences in the incoming angles of the scattered ejectiles. However this effect can be corrected for by plotting the entrance angle for the ejectiles as a function of the focal plane position and performing a linear correction to improve the spectrum resolution, as shown in Figure 4.14. In our experiment, we did not observe an explicit angular dependency on the
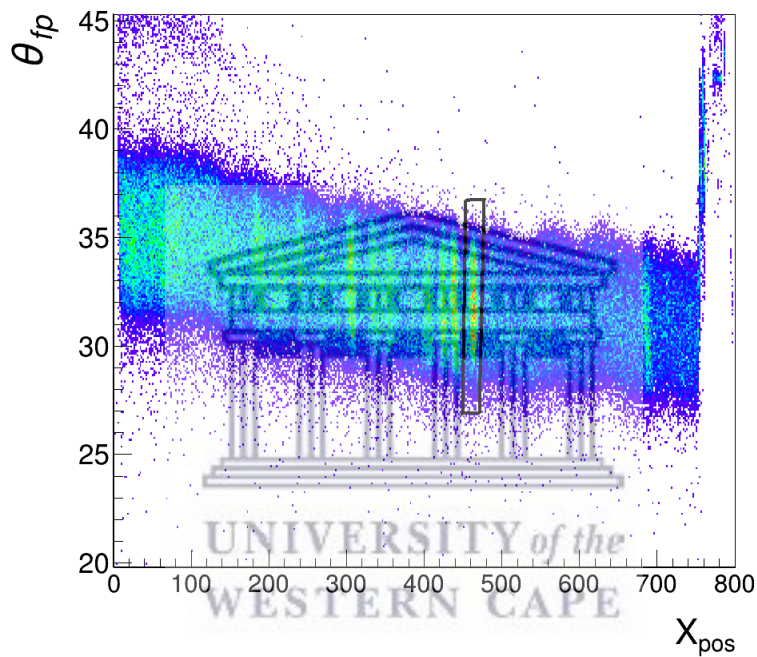
Figure 4.14: Triton focal plane entrance angles as a function of focal plane position. The selected locus corresponds to the 2859 keV state in the recoil.

resolution. This was most likely due to the dominant effects of triton energy losses within the target. A quick calculation confirms this assumption. For instance, tritons from the 2859 keV state in ^{32}Cl have kinetic energies in the range of 34.23 MeV $\leq E_t \leq$ 34.29 MeV for the two extreme emittance angles of $-2°$ and $2°$. This energy difference $\Delta E_\theta \sim 4.8$ keV is less than the energy loss for the tritons in the AgS target. We calculate the latter from the

61

Stopping and Range of Ions in Matter software (SRIM) [46]. The energy loss determination was from interpolated SRIM values as shown in Figure 4.15. The interpolation procedure used a code that iterated the energy loss over
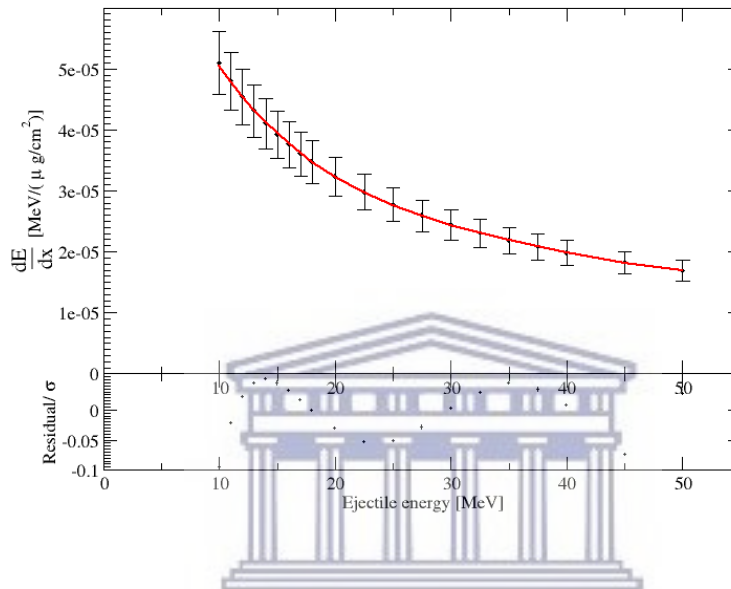
Figure 4.15: Triton energy loss in the AgS target as a function of the triton energy. The values are taken from SRIM with a conservative estimate of 10% relative uncertainty.

infinitesimal slices of target material. We extract the energy loss for the tritons from the 2859 keV state in the target to be $\Delta E_{Target} \sim 6.6$ keV.

4.3 Reaction and decay kinematics

We implemented a computer program to relativistically calculate the kinematics for the ^{32}S(^{3}He, t)^{32}Cl reaction, taking into consideration also the kinematics of the ^{32}Cl* proton-decay to a ^{31}S residual nucleus. The former follows the Oak Ridge National Laboratory kinematics code [47], whose algebra is briefly described below.

62

The Einstein's energy-momentum relation using natural units (i.e. $c = 1$) reads

$$E^2 = P^2 + m^2, \tag{4.9}$$

where E is the total energy, P is the momentum and m is the rest mass of a particle. Since we know the projectile and the target rest masses and kinetic energies, we can find the total energy of the ejectiles from the equation [47]

$$
\begin{aligned}
E_2 = \frac{1}{E_T^2 - P_0^2 \cos^2 \theta_2} \Bigg\{ &E_T \left(m_1 E_0 + \frac{m_0^2 + m_1^2 + m_2^2 + m_3^2}{2} \right) \\
&\pm P_0 \cos \theta_2 \Bigg[\left(m_1 E_0 + \frac{m_0^2 + m_1^2 + m_2^2 + m_3^2}{2} \right)^2 \\
&- m_2^2 m_3^2 - P_0^2 m_2^2 \sin^2 \theta_2 \Bigg]^{1/2} \Bigg\},
\end{aligned}
\tag{4.10}
$$

where the indices 0,1,2 and 3 denote the projectile, target, ejectile and recoil respectively. Here, $E_T = E_0 + E_1 = E_2 + E_3$ is the total energy of the system. Note that Eq. (4.10) above can have two solutions. The outcome is governed by the quantity

$$
\alpha = \frac{P_0}{E_T} \frac{1 + \frac{m_2^2 - m_3^2}{E_T^{'}}}{\left\{ \left[1 - \left(\frac{m_2 + m_3}{E_T^{'}} \right)^2 \right] \left[1 - \left(\frac{m_2 - m_3}{E_T^{'}} \right)^{1/2} \right] \right\}^{1/2}},
\tag{4.11}
$$

where, $E_T^{'} = \sqrt{m_0^2 + m_1^2 + 2m_1^2 E_0}$, is the total center of mass energy. If the quantity α is greater than 1, then two solutions are allowed for the scattering angle θ_2, and if $\alpha < 1$, only the positive sign term in Eq. (4.10) is a physically realistic solution [47]. Once we solve for the ejectile energy E_2, it is straightforward to find the recoil energy $E_3 = E_T - E_2$.

For the additional scenario where the recoil undergoes proton emission, we need to take into consideration that the recoil emits a proton while it is

63

in flight. With such an in-flight decay mode, the detected energy of the protons will be further lowered in the laboratory frame, as the CAKE array is positioned at backward angles in our measurement. This is illustrated in Figure 4.16. We can deduce the lab energy of the protons using the following
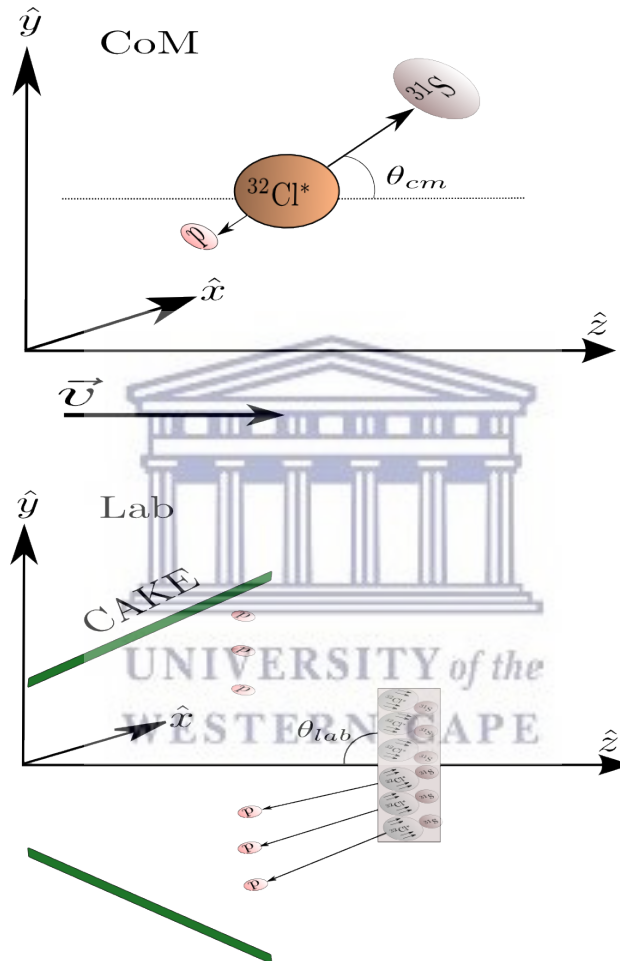
Figure 4.16: The decay of the recoil nuclease in the center of mass (CoM) and laboratory frames (Lab) of reference.

approach. In the rest frame of the $^{32}\text{Cl}^*$ recoil, prior to proton emission, the 4-momentum of the recoil is $P_3^{'} = (m_3, \vec{0})$, separated by the space and time components. After the break up of $^{32}\text{Cl}^*$ to $^{31}\text{S} + p$ (say in the ground state), the 4-momenta of the protons are $P_p^{'} = (E_p^{'}, \vec{p_p^{'}})$ and those of the residual ^{31}S

64

nuclei are $P_{res} = (E'_{res}, \vec{p}'_{res})$. The invariant mass of any particle is given by $E^2 - P^2 = M^2$. Momentum conservation requires that $\vec{p}'_p = -\vec{p}'_{res}$. Furthermore, we also have

$$P'_3 = P'_p + P'_{res}. \tag{4.12}$$

We can then rewrite the above as

$$P'_{res}{}^2 = (P'_3 - P'_p)^2 = P'^2_3 + 2P'_3.P'_p + P'^2_p, \tag{4.13}$$

which yields

$$m^2_{res} = m^2_3 - 2m_3 E'_p + m^2_p \implies E'_p = \frac{m^2_3 + m^2_p - m^2_{res}}{2m_3}, \tag{4.14}$$

and

$$E'_{res} = \frac{m^2_3 + m^2_{res} - m^2_p}{2m_3}. \tag{4.15}$$

Substituting the above into Eq. (4.9), we get

$$p'_p = \frac{\sqrt{(m^2_3 + m^2_p - m^2_{res})^2 - 4m^2_p m^2_3}}{2m_3}, \tag{4.16}$$

similarly

$$p'_{res} = \frac{\sqrt{(m^2_3 + m^2_{res} - m^2_p)^2 - 4m^2_{res} m^2_3}}{2m_3}. \tag{4.17}$$

Now lets assume that the beam and the ^{32}Cl recoil are along the $+\hat{z}$ direction as shown in Figure 4.16. Then the proton emission would occur in the xy plane. If the protons are emitted at an arbitrary angle of θ_{cm} to the direction of motion in the rest frame of the ^{32}Cl nucleus, the longitudinal and transverse

65

momenta for the protons are simply

$$p'_{p\perp} = p'_p \sin\theta_{cm}, \tag{4.18}$$

and

$$p'_{pz} = p'_p \cos\theta_{cm}. \tag{4.19}$$

The latter value can be transformed to the laboratory frame by a Lorentz boost

$$p_{pz} = \gamma(p'_{pz} + vE'_p), \tag{4.20}$$

with $\gamma = \frac{E_3}{m_3}$ and $v = \frac{P_3}{E_3}$. Similarly,

$$E_p = \gamma(E'_p + vp'_{pz}). \tag{4.21}$$

4.4 Coincidences between CAKE and the focal plane events

Particles detected in CAKE are defined by a unique pair of a triggered ring and sector, that together define a pixel, as shown in Figure 4.17. Furthermore, when ejectiles are detected at the focal plane, signals from the scintillator paddle trigger the K600 DAQ-system to acquire data. The paddle also generates an ~ 6 μs-wide ADC gate signal. Consequently, for the coincidences to occur, the CAKE energy signals fed to the ADCs must also be registered within this time period. However, this time window is long enough that uncorrelated events could be triggered on multiple rings and sectors in CAKE. Such scenario leads to a wrong position information registered on the DSSSDs. Furthermore, if a particle is incident on CAKE in the vicinity of

66
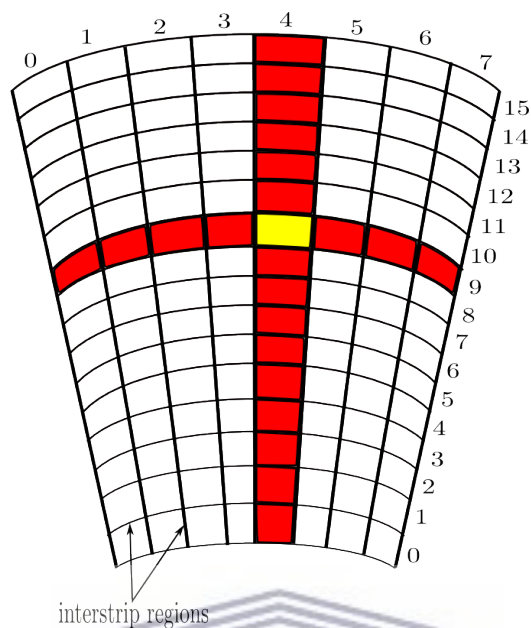
Figure 4.17: A schematic of one DSSSD of CAKE. The particle hits the DSSSD at the yellow pixel and triggers the channels of ring 9 and sector 4.

the inter-strip regions in the DSSSD (see Figure 4.17), it would also trigger a neighbouring pixel. To avoid this, we implemented a restriction rule in the data sorting code to select valid events to be accepted only if

$$\left| \sum_{pixel=0}^{16} E_{ring} - \sum_{pixel=0}^{8} E_{sector} \right| < 300 \text{ keV}. \tag{4.22}$$

The above implies that the energy difference by a valid event in a whole ring $\sum E_{ring}$ and sector $\sum E_{sector}$ must not exceed 300 keV. This condition eliminates events from multiple hits on a ring or a sector. The effects of this restriction rule are shown in Figures 4.18 and 4.19.

67
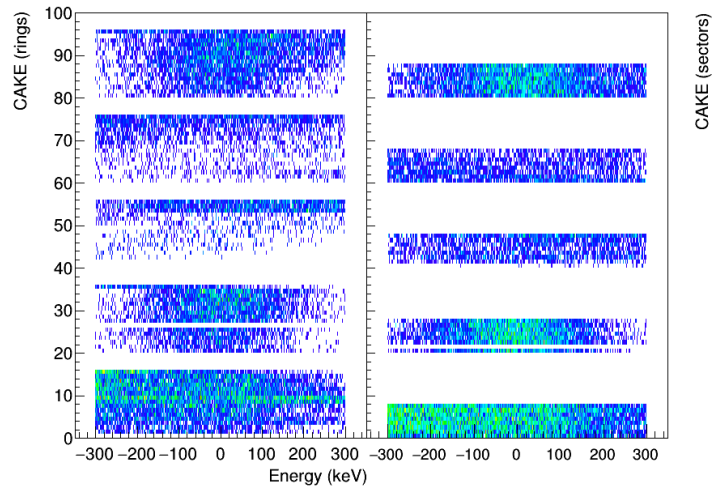
Figure 4.18: Left panel: Counts in the rings as a function of the energy difference between the sector and the ring pair. Right panel: Sector counts as a function of the energy difference between the sector and the ring pair.
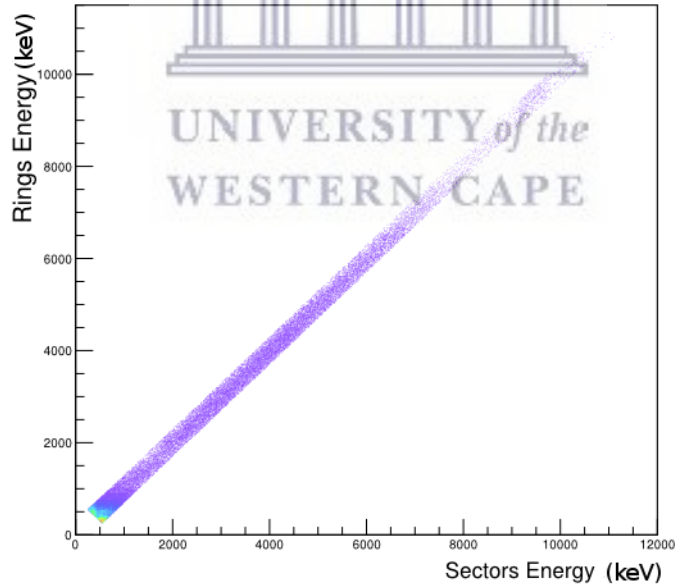
Figure 4.19: E_{ring} vs E_{sector}, with the restriction rule from equation (4.22) applied.

68

4.5 Angular distribution of the protons

As mentioned previously, the total angular momentum and the parity (J^π) of proton-unbound states can be determined by the angular distribution of the decay protons in CAKE. Furthermore the measured proton branches from astrophysically relevant states in ^{32}Cl would allow an independent determination of the ^{31}S(p, γ) reaction rate. However, a realistic estimation of the proton branches (and hence Γ_p) can only be made if the angular distribution of the protons is incorporated in the calculation. Unfortunately, as seen in Figure 4.13, the proton yields measured by our experiment were too low to perform such an analysis for this particular case. Nevertheless, below we develop the algebra for such angular distribution measurements, which would be useful for future similar investigations. Since the spectrometer was configured to acquire data in the zero degree mode, with the ejectiles detected at $-2°$ to $2°$ acceptance angle, one can use γ-ray angular correlation techniques, developed by Litherland & Ferguson and denoted by Method II [48], which we describe below.

Assume the $(^3$He$, t)$ reaction to produce a final state in ^{32}Cl (with spin and parity J^π), which further undergoes proton emission, leaving the residual ^{31}S nucleus in the ground state. This is shown in Figure 4.20. The incoming channel spin for the reaction is easily obtained from a vector addition of the spins of the ^{3}He projectile and the ^{32}S target

$$S_{projectile} \otimes S_{target}. \tag{4.23}$$

69
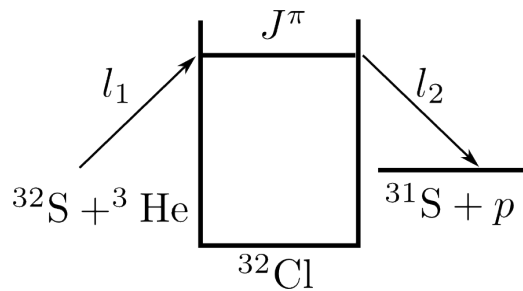
Figure 4.20: Incoming and outgoing channel spins for $^{32}\text{S}(^3\text{He}, t)^{32}\text{Cl}^*(p)$.

Similarly, for the outgoing channel spin, where the ^{32}Cl recoil decays to $^{31}\text{S} + p$, the spin coupling is

$$S_{residual} \otimes S_{proton}. \tag{4.24}$$

This restricts the incoming channel spin to $\frac{1}{2}$ and the outgoing channel spin to either $S = 0^+$ or $S = 1^+$. From the above, the state labelled by $|J^\pi\rangle$ in the ^{32}Cl nucleus can only be formed by the addition of the angular momentum of the incoming spin channel and the orbital angular momentum of the incident beam $\vec{l_1}$, so that

$$J = \frac{1^+}{2} \otimes \vec{l_1}. \tag{4.25}$$

Similarly, break up of the ^{32}Cl nucleus can be described by either of the two angular momentum couplings

$$0^+ \otimes \vec{l_2} = J, \tag{4.26}$$

or

$$1^+ \otimes \vec{l_2} = J, \tag{4.27}$$

where $\vec{l_2}$ is the orbital angular momentum for the emitted proton.

As mentioned before, since the outgoing tritons are detected at 0°, with a

70

small acceptance angle window for the spectrometer, this is similar to having an axially symmetric detector at zero degrees. This implies that the orbital angular momentum from the incoming beam has no contribution for proton focal plane coincidences. Therefore, the populated substates of $|J\rangle$ can not exceed the following spin addition

$$|m_{max}| = S_{beam} + S_{target} + S_{ejectile}. \qquad (4.28)$$

This is essentially the crux of Method II by Litherland & Ferguson, where the process of measuring particle coincident events using an axially symmetric counter at $0°$ or $180°$ greatly restricts the m-state population of $|J^\pi\rangle$. Consequently, for our case this results in $|m_{max}| = \frac{1}{2} + 0 + \frac{1}{2} = 1$. Therefore, only $m = 0, \pm 1$ substates are populated for all $|J\rangle$ by the ${}^{32}\text{S}({}^{3}\text{He}, t){}^{32}\text{Cl}$ reaction. This restriction on the alignment of the final state is a useful constraint. Assuming that the $m = 0$ and $m = \pm 1$ sub-states are symmetrically populated [49] as shown in Figure 4.21, we can write this **constraint** as the sum of population fractions

$$P(m = 0) + 2P(m = 1) = 1. \qquad (4.29)$$

This unequal population of the m-states results in a non-isotropic angular distribution for the emitted protons. The experimental angular distribution is expected to be of the form

$$W(\theta) = \sum_{k=even} A_k P_k(\cos\theta), \qquad (4.30)$$

71
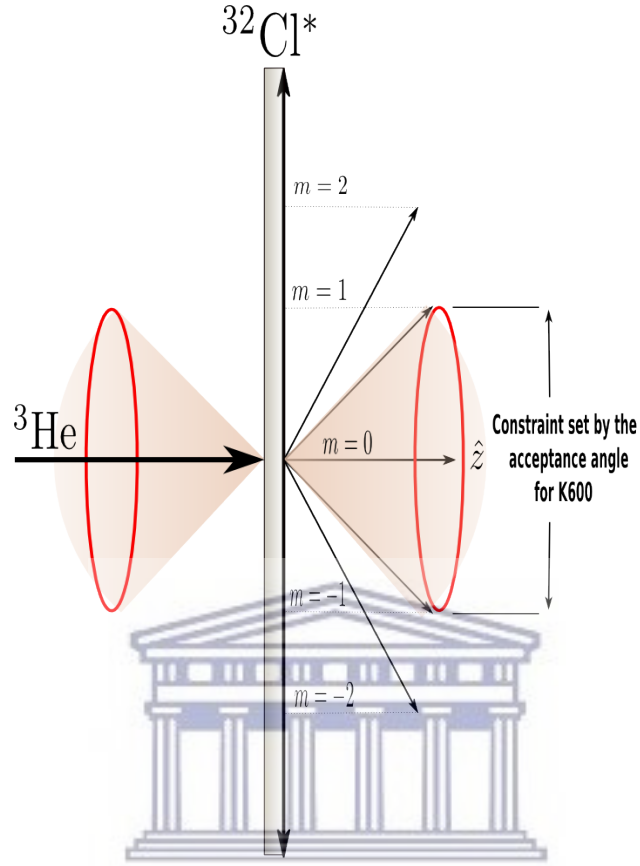
Figure 4.21: Angular momentum projection along beam axis, the axial symmetry defined by the spectrometer acceptance angle.

where the A_k coefficients are

$$A_k = \sum_{mSll'} P(m)\langle JmJ{-}m|k0\rangle(-)^{S-m}\overline{Z}(lJl'J;Sk) \times \langle J||l||S\rangle\langle J||l'||S\rangle^*.$$

(4.31)

The Clebsch Gordan $\langle JmJ{-}m|k0\rangle$ and the $\overline{Z}$ coefficients above are defined in Ref. [48]. Furthermore, the sum runs over allowed values of the channel spin S, and two allowed values of the orbital angular momentum l and l'. The reduced matrix element $\langle J||l||S\rangle$ represents a decay from a state with total angular momentum J to a channel spin S, with orbital angular momentum l.

72

Parity conservation demands that two different l values are allowed only if $l' = l + 2$. This is the **second constraint**. Therefore there can only be s-wave and d-wave mixing (p-wave and f-wave mixing etc) for the different l values of the protons. This constraint does not allow combinations of $l = 0$ and $l = 1$ orbital momentum values for example.

The $\overline{Z}(lJl'J; Sk)$ coefficients in Eq. (4.31) can be rewritten as

$$\overline{Z}(lJl'J; Sk) = \frac{1}{\sqrt{2l+1}} \frac{1}{\sqrt{2l'+1}} \langle l0l'0|k0 \rangle W(lJl'J; sk), \qquad (4.32)$$

where $W(lJl'J; sk)$ is the Racah W coefficient defined by

$$W(lJl'J; sk) = (-)^{l+l'+2J} \begin{Bmatrix} l & J & S \\ J & l' & k \end{Bmatrix}. \qquad (4.33)$$

The quantity in the matrix above is the Wigner $6j$ coefficient. It should also be noted the the $\langle l0l'0|k0 \rangle$ Clebsch Gordan coefficient in Eq. (4.32) is only non-zero when $k =$ even, for parity conservation to hold. This is because if $l' = l + 2$, then k can only take values between 2 and $(2l + 2)$. This is the **third constraint** (see Eq. 4.30).

Now lets assume that the state $|J^\pi\rangle$ is a natural parity state defined by $\pi_{initial} = (-1)^J$. As mentioned previously, the possible outgoing channel spins for this state can only be 0^+ or 1^+. Therefore, we have the following possibilities

$$S = 0: \qquad \text{Then } J \text{ can only be} \qquad J = l. \qquad (4.34)$$

$$S = 1: \quad \text{Then } J \text{ can only take values} \quad J = l, l \pm 1. \qquad (4.35)$$

73

The final state is $|^{31}\mathrm{S}\rangle \otimes |p\rangle$ and its parity is $\pi_{final} = (+)(+)(-1)^l$ (as it is a multiplicative quantum number). As parity needs to be conserved, we have the following results. For the possibility that $J = l$, $\pi_{initial} = (-1)^J = (-1)^l = \pi_{final}$. However, for the other possibility $J = l \pm 1$, the allowed π_{final} value has to be $\pi_{final} = (+)(+)(-1)^J(-1)^{\pm 1}$ which is not equal to $\pi_{initial}$. So the $J = l \pm 1$ is forbidden. Similarly if $|J^\pi\rangle$ were unnatural parity states, so that $\pi_{initial} = (-1)^{J+1}$ then only the values of $l = J \pm 1$ are allowed, while the $l = J$ values are forbidden for the protons. These selection rules make the **fourth constraint** for the proton analysis.

The **last constraint** arises from the $\langle JmJ - m|k0\rangle$ Clebsch Gordon coefficient, which requires that $A_k = 0$ if $k > 2J$. This limits the total number of terms in Eq. (4.30).

Given enough statistics in the coincidence spectrum, the above constraints allow an analysis of the protons' (or other charged particles) angular distribution using the CAKE array, once the efficiency of each strip is known. The latter can be easily determined using a GEANT simulation. This has already been performed in another Master's project [38].

74

Chapter 5

Conclusions and future work

In conclusion, we have investigated (mainly) proton unbound states in ^{32}Cl with a ^{32}S(^{3}He, t) charge-exchange reaction. One goal of this measurement was to search for potential sources of isospin mixing that would lead to a violation of the IMME in the $A = 32$, $T = 2$ quintet. The other goal was to indirectly determine the ^{31}S(p, γ) reaction rate, which is an important reaction for nucleosynthesis in explosive stellar environments. In our experiment we identify a previously unknown state in ^{32}Cl at an excitation energy of 4983(3) keV. This state is separated from the $T = 2$ isobaric analogue state in ^{32}Cl at 5046 keV by an energy difference of $\Delta E = 63$ keV. If this state were 0^+ in nature, then it is possible that it would be a source of isospin mixing, which would in turn explain the IMME violation for the $A = 32$, $T = 2$ quintet. Regrettably, the proton-focal plane coincident spectra from this experiment did not have enough statistics to perform an angular distribution measurement and obtain the spin-parity of the 4983(3) keV state. This was mainly due to the low cross section for the (^{3}He, t) reaction, which we determine to be approximately 0.1 mb. Nevertheless, assuming that the state was 0^+ in nature, we can make estimations based on a two-state mix-

ing picture. Using the formula derived in Eq. (1.19) and further assuming a mixing matrix element of approximately 20 keV, based on the calculations of Signoracci and Brown [13], we obtain the unperturbed energy difference between the two states to be ≈ 48.7 keV. This means that the $T = 2$ state would be shifted upwards by ≈ 7 keV, assuming purely two-state mixing. Consequently, the mass excess of the $T = 2$ state in ^{32}Cl should be corrected to $M = -8287.84(70)$ keV prior to performing the IMME fit. With other measured masses, a quadratic fit to the IMME with this value unfortunately does not resolve the issue. In fact, we obtain a reduced χ^2 value of 32.4 for a quadratic fit to the masses. So it is highly possible that

1. The 4983 keV state is not a 0^+ state as expected, or

2. There are unaccounted systematic effects that might have affected some of the mass measurements.

This requires further investigation.

The low statistics in the coincidence data also affected our planned $\left(\frac{\Gamma_p}{\Gamma}\right)$ measurement to obtain the ^{31}S(p, γ) reaction rate. Nonetheless, despite the above, we have algebraically developed a procedure to analyse the proton angular distributions in such data, taking advantages of certain constraints set by angular momentum selection rules and other conservation laws. For future similar experiments that have a high cross section for CAKE-focal plane coincidences, we can take advantage of this procedure to effectively use Method II of Litherland & Ferguson, together with a χ^2 minimization technique in order to determine possible l values for a given proton branch. Once the transferred l for a proton group is determined, extracting the J^π of the unbound states should be trivial.

76

Bibliography

[1] Ernest M Henley and Alejandro Garcia. *Subatomic physics*. World Scientific, 2007.

[2] Nouredine Zettili. Quantum mechanics: concepts and applications, 2003.

[3] Fay Ajzenberg-Selove. Energy levels of light nuclei $A = 13 - 15$. *Nuclear Physics A*, 523(1):1–196, 1991.

[4] DH Wilkinson. Isospin in nuclear physics. *North-Holland, Amsterdam*, 1969.

[5] WE Ormand. Mapping the proton drip line up to $A = 70$. *Physical Review C*, 55(5):2407, 1997.

[6] WA Richter and B Alex Brown. Shell-model studies of the astrophysical rp reaction ^{29}P(p, γ)^{30}S. *Physical Review C*, 87(6):065803, 2013.

[7] John C Hardy and IS Towner. Superallowed $0^+ \rightarrow 0^+$ nuclear β decays: A new survey with precision tests of the conserved vector current hypothesis and the standard model. *Physical Review C*, 79(5):055502, 2009.

[8] R Casten. *Nuclear structure from a simple perspective*, volume 23. Oxford University Press, 2000.

[9] M Brodeur, T Brunner, S Ettenauer, A Lapierre, R Ringle, BA Brown, D Lunney, and J Dilling. Elucidation of the anomalous $A = 9$ isospin quartet behavior. *Physical Review Letters*, 108(21):212501, 2012.

[10] AA Kwiatkowski, BR Barquest, G Bollen, CM Campbell, DL Lincoln, DJ Morrissey, GK Pang, AM Prinke, J Savory, S Schwarz, et al. Precision test of the isobaric multiplet mass equation for the $A = 32, T = 2$ quintet. *Physical Review C*, 80(5):051302, 2009.

[11] A Kankainen, T Eronen, D Gorelov, J Hakala, A Jokinen, VS Kolhinen, M Reponen, J Rissanen, A Saastamoinen, V Sonnenschein, et al. High-precision mass measurement of ^{31}S with the double penning trap improves the mass value for Cl. *Physical Review C*, 82(5):052501, 2010.

[12] M MacCormick and G Audi. Evaluated experimental isobaric analogue states from $T = \frac{1}{2}$ to $T = 3$ and associated IMME coefficients. *Nuclear Physics A*, 925:61–95, 2014.

[13] Angelo Signoracci and B Alex Brown. Effects of isospin mixing in the $A = 32$ quintet. *Physical Review C*, 84(3):031301, 2011.

[14] Gary Steigman. Primordial nucleosynthesis in the precision cosmology era. *Annu. Rev. Nucl. Part. Sci.*, 57:463–491, 2007.

[15] Claus E Rolfs and William S Rodney. *Cauldrons in the cosmos: Nuclear astrophysics.* University of Chicago press, 1988.

[16] Christian Iliadis. *Nuclear physics of stars.* John Wiley & Sons, 2015.

[17] `https://commons.wikimedia.org/wiki/File:Evolved_star_` `fusion_shells.svg`.

[18] Huan Yang, Vasileios Paschalidis, Kent Yagi, Luis Lehner, Frans Pretorius, and Nicolás Yunes. Gravitational wave spectroscopy of binary neutron star merger remnants with mode stacking. *Physical Review D*, 97(2):024049, 2018.

[19] `https://scienceborealis.ca/`.

[20] Jordi José. Stellar pyrotechnics: Nucleosynthesis in classical novae & X-ray bursts. *Nuclear Physics A*, 752:540–549, 2005.

[21] E Margaret Burbidge, Geoffrey Ronald Burbidge, William A Fowler, and Fred Hoyle. Synthesis of the elements in stars. *Reviews of modern physics*, 29(4):547, 1957.

[22] AGW Cameron. Atomic energy of Canada. *Ltd., CRL-41*, 1957.

[23] John Markus Blatt and Victor Frederick Weisskopf. *Theoretical nuclear physics*. Courier Corporation, 1991.

[24] Thomas Matheson, Alexei V Filippenko, and Luis C Ho. Nova herculis 1991: thermonuclear runaway on a massive ONeMg white dwarf. *The Astrophysical Journal*, 418:L29, 1993.

[25] M Dopita, S Ryder, E Vassiliadis, T Kato, and R Hirata. Nova herculis 1991. *International Astronomical Union Circular*, 5262, 1991.

[26] Shinya Wanajo, Masa-aki Hashimoto, and Ken'ichi Nomoto. Nucleosynthesis in ONeMg novae: models versus observations to constrain the masses of onemg white dwarfs and their envelopes. *The Astrophysical Journal*, 523(1):409, 1999.

79

[27] C Jeanperrin, LH Rosier, B Ramstein, and EI Obiajunwa. Spectroscopy of ^{32}Cl nucleus via the ^{32}S(^{3}He, t)^{32}Cl reaction at 34.5 MeV. *Nuclear Physics A*, 503(1):77–89, 1989.

[28] M Matoš, Jeff C Blackmon, LE Linhardt, Daniel W Bardayan, Caroline D Nesaraja, JA Clark, CM Deibel, PD OMalley, and PD Parker. Unbound states of ^{32}Cl and the ^{31}S(p, γ)^{32}Cl reaction rate. *Physical Review C*, 84(5):055806, 2011.

[29] C Wrede, JA Clark, CM Deibel, T Faestermann, R Hertenberger, A Parikh, H-F Wirth, S Bishop, AA Chen, K Eppinger, et al. Properties of ^{20}Na, ^{24}Al, ^{28}P, ^{32}Cl, and ^{36}K for studies of explosive hydrogen burning. *Physical Review C*, 82(3):035805, 2010.

[30] C Wrede, A García, D Melconian, S Triambak, and BA Brown. γ-ray constraints on the properties of unbound ^{32}Cl levels. *Physical Review C*, 86(4):047305, 2012.

[31] M Bhattacharya, D Melconian, A Komives, S Triambak, A Garcia, EG Adelberger, BA Brown, MW Cooper, T Glasmacher, Valdir Guimaraes, et al. ft value of the $0^+ \rightarrow 0^+ \beta^+$ decay of ^{32}Ar : A measurement of isospin symmetry breaking in a superallowed decay. *Physical Review C*, 77(6):065503, 2008.

[32] L Afanasieva, JC Blackmon, CM Deibel, J Lai, LE Linhardt, BC Rasco, D Seweryniak, M Alcorta, MP Carpenter, JA Clark, et al. γ spectroscopy of states in ^{32}Cl relevant for the ^{31}S(p, γ)^{32}Cl reaction rate. *Physical Review C*, 96(3):035801, 2017.

[33] P Adsley, R Neveling, P Papka, Z Dyers, JW Brummer, C Aa Diget, NJ Hubbard, KCW Li, A Long, DJ Marin-Lambarri, et al. CAKE: The

coincidence array for K600 experiments. *Journal of Instrumentation*, 12(02):T02004, 2017.

[34] R Neveling, H Fujita, FD Smit, T Adachi, GPA Berg, EZ Buthelezi, J Carter, JL Conradie, M Couder, RW Fearick, et al. High energy-resolution zero-degree facility for light-ion scattering and reactions at ithemba labs. *Nuclear Instruments and Methods in Physics Research Section A: Accelerators, Spectrometers, Detectors and Associated Equipment*, 654(1):29–39, 2011.

[35] R Neveling, FD Smit, H Fujita, and RT Newman. Guide to the K600 magnetic spectrometer, 2009.

[36] John P Greene and Christopher J Lister. The production of sulphur targets for γ-ray spectroscopy. *Nuclear Instruments and Methods in Physics Research Section A: Accelerators, Spectrometers, Detectors and Associated Equipment*, 480(1):79–83, 2002.

[37] DD Watson. Simple method for making sulfur targets. *Review of Scientific Instruments*, 37(11):1605–1606, 1966.

[38] Kevin Ching Wei Li. *Characterization of the pre-eminent 4-α cluster state candidate in ^{16}O*. 2015.

[39] Emil Kowalski. *Nuclear electronics*. Springer-Verlag, 2013.

[40] Jacobus Andreas Swartz. *Search for low-spin states above the 5-α break-up threshold in ^{20}Ne*. PhD thesis, Stellenbosch: Stellenbosch University, 2014.

[41] `https://www.nndc.bnl.gov/`.

81

[42] `https://sourceforge.net/projects/nukesim-classes/`.

[43] Smarajit Triambak. *The isobaric multiplet mass equation and ft value of the 0^+ going to 0^+ Fermi transition in ^{32}Ar: Two tests of isospin symmetry breaking.* PhD thesis, 2007.

[44] `https://root.cern.ch/doc/v608/FitUtil_8cxx_source.html#l00474`.

[45] `https://www.nndc.bnl.gov/ensdf/`.

[46] `http://www.srim.org/`.

[47] RE Phillips and ST Thornton. A FORTRAN program for relativistic kinematic calculations in two-body nuclear reactions. Technical report, Oak Ridge National Lab., Tenn., 1967.

[48] AE Litherland. AE Litherland and AJ Ferguson, Can. J. Phys. 39, 788 (1961). *Can. J. Phys.*, 39:788, 1961.

[49] JW Noé, DP Balamuth, and RW Zurmühle. Angular correlation study of the proton decay of ^{14}N states below 11 MeV. *Physical Review C*, 9(1):132, 1974.

82